Coordination Chemistry Reviews 253 (2009) 2852–2871

Contents lists available at ScienceDirect

Coordination Chemistry Reviews

journal homepage: www.elsevier.com/locate/ccr

Review

Transition metal and nitrogen doped carbon nanostructures

Stanislav R. Stoyanov[a,b], Alexey V. Titov[a], Petr Král[a,*]

[a] Department of Chemistry, University of Illinois at Chicago, Chicago, IL 60607, USA
[b] National Institute for Nanotechnology, National Research Council of Canada and Department of Mechanical Engineering, University of Alberta, Edmonton, AB, Canada

Contents

ARTICLE INFO

Article history:
Received 21 January 2009
Accepted 11 March 2009
Available online 24 March 2009

Keywords:
Nanotube
Nanocone
Nanocapsule
Doping

ABSTRACT

We review our theoretical first-principle studies of carbon nanostructures based on graphene sheets, carbon nanotubes, nanocones and fullerenes that are substitutionally doped with transition metal and nitrogen atoms. The results obtained show that metal doping leads to more stable systems in buckled rather than planar structures. The hybrid structures have low-lying excited states, allowing for catalytic activity, in analogy to metalloporphyrins and metallophthalocyanines, as confirmed in recent experiments with Fe-xN-doped carbon nanotubes. Metal-doped carbon nanocones and nanocapsules based on typical fullerenes manifest remarkable electronic and spin polarizations. Additional doping by boron atoms adjacent to the metals increases their HOMO–LUMO gap, stabilizes their electronic structures and causes that their ground states have higher spin multiplicity, where the spin density is spread over the systems. The

* Corresponding author at: Department of Chemistry, University of Illinois at Chicago, 845 W Taylor St, Room 4500 SES, Chicago, IL 60607, United States.
E-mail address: pkral@uic.edu (P. Král).

0010-8545/$ – see front matter
doi:10.1016/j.ccr.2009.03.011

Metal
Graphene

metallic sites allow functionalization and potential activation of these nanosystems. The hybrid structures formed can have a broad range of applications in catalysis, molecular electronics, light-harvesting and nanomechanics.

1. Introduction

Carbon fullerenes [1–3], nanotubes [4–6], nanocones [7,8] and graphene [9–11] have unique mechanical and electronic properties, since they possess rigid skeletons formed by bonded planar sp^2 molecular orbitals (MO) sandwiched between overlapping unsaturated π MOs [12]. All these types of carbon nanostructures can be doped by boron, nitrogen and other atoms in order to change their electronic properties [13–16] or form chemically active local sites [17–21]. Perhaps, the simplest way how to functionalize these systems is to attach the potential ligands to the nanostructure perifery. For example, one can anchor nucleotides at the CNT rims [22]. When all the C atoms are replaced, BN nanotubes [23,24] and nanocapsules [25] can be formed that are photoactive and piezoelectric [26,27]. Carboneous nanostructures can be also chemically modified to gain other activities [28–30]. Functionalized by physisorption [31] and covalent bonding [32], these hybrid systems can be used in molecular sensing [33], controlling [34] or drug delivering [35].

Particularly attractive is the possibility of developing stable metal-doped carbon nanostructures for catalytic applications. Early experiments observed the catalytic activity of Co-phtalocyanines [36] and motivated further studies of transition metal(Fe,Co)-nitrogen-carbon catalysts [37–42]. In particular, Dodelet et al. [43,40,44] have investigated catalysts based on Fe and Co adsorbed on nitrogen-modified carbon supports, which were obtained by high-temperature pyrolysis using a variety of precursors. It was found that the increase of N content in the $Fe_xC_{1-x-y}N_y$ carbon support materials promotes the incorporation of dispersed metal atoms, which leads to an increase in catalytic activity. Recently, it was also suggested that nitrogenated CNTs arrays might have unusually high electrocatalytic activity for oxygen reduction [45].

Techniques for N-doping of carbon nanostructures were discussed by Ewels and Glerup [46]. Nitrogen atoms bonded to 2–3 C atoms in carbon nanotubes (CNTs) have been observed experimentally by Terrones et al. [47], where the N atoms form 3 stable pyridine-like substitution sites and vacancies in the CNT walls. They have also demonstrated that N-mediated growth of CNTs leads to diameter reduction, tube closures and promotes the formation of bamboo-like structures [48]. Carbon nanocones with "open" pocket-like structures and "spike-like" tips might be especially suitable for functionalization leading to rich potential applications. Their tips have been, for example, functionalized by oxidation and subsequent deposition of Gd atoms [49]. Nitrogen-doped carbon nanocups (nanobells) self-aggregates by hydrogen bonding and coordinate to gold nanoparticles through the rim N atoms [50,51]. It would be potentially interesting to form universal binding sites on these structures allowing stable chemical, electronic and mechanical connectivity to different types of ligands.

In this work, we review our recent studies devoted to this problem, realized by substitutional metal–nitrogen doping of carbon nanostructures. When we started to search for stable metal–nitrogen complexes that might form in carbon nanostructures, we turned our attention to *metalloporphyrins*. These highly stable systems formed in nature gain their universality from a central metal site coupled to several connected pyrrole rings [52]. Metalloporphyrins, with Fe in different oxidation states, can easily undergo redox reactions in living systems and activate many biochemical reactions [53,54]. They could be used as matrices for hydrogen storage [55] and optical devices [56,57]. Porphyrins can be part of square planar as well as octahedral complexes that have been thoroughly investigated [58,59]. Recently, porphyrin-based nanostructures, such as nanotapes [60] or nanochannels [61,62] have also been discussed.

After some preliminary calculations, we have been able to show that transition metal atoms coordinated to 3–4 N atoms could be integrated into carbon nanocones by substituting a similar number of C atoms [63–65]. In this way, *metallic binding sites* could be formed in carboneous nanostructures and further functionalized. Moreover, external electric fields could easily control the attachment of ligands to and their release from metal-doped carbon nanostructures [66].

We organize this review as follows. In Section 2, we briefly discuss theoretical methods used. In Section 3, we theoretically examine the possibility of integrating metalloporphyrine-like centers into graphene sheets and CNTs [65]. In Section 4, we show how such centers can be formed in carbon nanocones [63]. In Section 5, we discuss formation of single and multi-metallic centers in fullerenes [64]. In Section 6, we explore several potential application of these substitutionally-doped nanostructures in the fields of catalysis [65] and controlled ion adsorption [66], light-harvesting and nanomechanics [64]. We conclude this Review in Section 7.

2. Computational methods

We describe the electronic structures and properties of the metal-doped carbon nanostructures by first-principle techniques at the Density Functional Theory (DFT) level [67]. We calculate their optimized geometries using the B3LYP exchange-correlation functional [68], implemented in the Gaussian03 software package (G03) [69], which successfully accounts for the relative changes in metal-ligand distances [70–73]. For the main-group atoms and first row transition metal atoms, we use the all-electron double-ζ6-31G*[74], triple- ζ6-311G*or 6-311G** basis sets, respectively [75–78]. For the heavy transition metal atoms Ru, Re, Os, Th, and Ce, we apply the Stuttgart–Dresden (SDD) effective core potentials (ECP) for the core electrons and the SDD basis set for the valence electrons [79,80]. In the computationally intense modeling of extended electronic states under external electric field, we employ the SDD ECP for the Ni atom core electrons and the SDD basis set for the valence electrons [79,80], whereas for the main-group atoms, we use the all-electron double- ζ3-21G$^{(*)}$basis set [81]. Closed-shell and open-shell calculations are performed using single and double determinants, respectively. Wiberg bond orders are calculated using Natural Bond Orbital (NBO) [82]. For comparison, we perform optimizations of these structures also with the Amsterdam Density Functional (ADF) [83–87], where we use the Generalized Gradient Approximation (GGA) and the BLYP exchange-correlation functional. For all the atoms, we utilize the TZP basis set that is similar to the triple- ζ6-311G*in Gaussian 03. We also use the *ab initio* multiple scattering model of extended X-ray absorption Fine Structure (EXAFS) implemented in FEFF 7.0 package [88].

3. Metal-doped graphene and carbon nanotubes

In this section, we review the material obtained in the recent studies [65]. We discuss the optimized geometries and electronic structures of transition metal and nitrogen doping sites formed in graphene monolayers and CNTs.

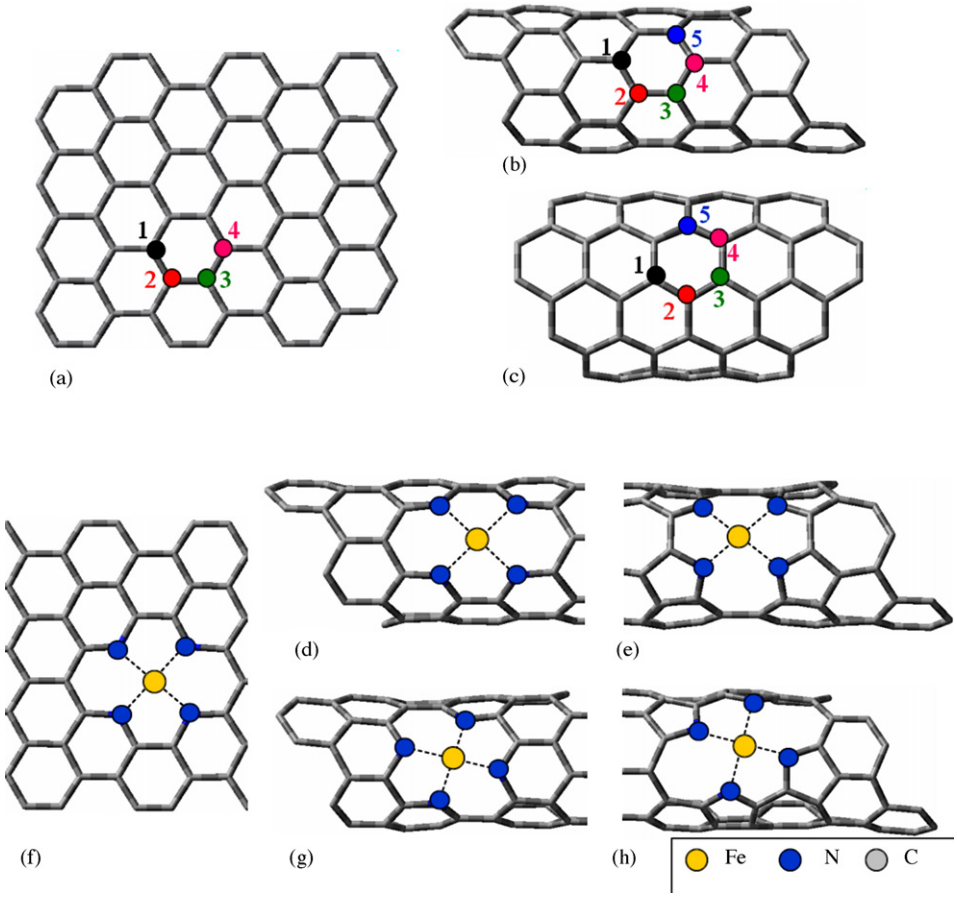

Fig. 1. (top) Nitrogen atom substitution into (a) planar graphene, (b) (7,0) CNT, and (c) (5,5) CNT. (bottom) The Fe–4N substitution sites for (f) graphene sheet and (d,e,g,h) (7,0) CNT clusters. Coordinations of Fe to pyridine-like and pyrrole-like configurations are shown in (d,g) and (e,h), respectively. The configurations are in axial (d,e) and helical orientations (g,h). Terminal hydrogen atoms are not shown.

3.1. Fe-xN clusters embedded in carbon nanostructures

The model systems formed by Fe-xN embedded in graphene and CNTs are modeled at the DFT/B3LYP/6-31G*level. A cluster approach is chosen to construct models of the active site incorporated into graphene sheets or CNTs [65]. In order to analyze in the calculations the effect of curvature of the CNTs, we use bent clusters cut from the nanotubes, with edge carbon atoms terminated by hydrogen atoms. To maintain the desired surface curvature, hydrogens at the edges of the clusters are kept fixed during the optimization of the molecular geometry. The cluster models of the planar graphene, shown in Fig. 1 (a), and the zigzag (8,0) CNT (not shown) contain 24 fused six-membered rings. The clusters representing (7,0) CNT and the (5,5) CNT contain 23 fused six-membered rings, respectively, as we show in Fig. 1(b) and (c).

We have studied clusters containing Fe coordinated to two and four N atoms, denoted as Fe–2N and Fe–4N, respectively [65]. Three-nitrogen structures were not studied, since there is no experimental evidence for their stability. The cluster models of CNTs and graphene with the enumeration of their atoms that is used in nitrogen substitution notations are shown in Fig. 1(a–c). The ground electronic states of the Fe–2N and Fe–4N clusters are singlet and triplet, respectively [65].

In the graphene sheet (Fig. 1(a)), each pair of carbon atoms labeled 1-2, 1-3 and 1-4 is substituted by two N atoms to obtain the corresponding 2N structure. In the CNT fragments (Fig. 1(b and c)), the axial symmetry of the nanotubes introduces three additional nonequivalent configurations. In total, the CNT fragments have six configurations along the symmetry axis and at various angles to it, respectively. We call a Fe–2N configuration *axial* (AX), if the axis containing the nitrogen atoms is parallel to the nanotube axis, and *helical* (HE) in all other cases. Thus, zigzag CNT clusters have axial configurations (2-3) and (1-4) for the nearest neighbor and the third-nearest neighbor nitrogen atoms, respectively. In addition, the zigzag (7,0) CNT in Fig. 1(b) has four HE configurations: the nearest neighbor (1-2), the next-nearest neighbor (2-4) and (3-5) and the third-nearest neighbor configurations (2-5). The armchair (5,5) CNT in Fig. 1(c) has one AX and five HE configurations: (1,3), (1,2), (1,4), (1,5), (2,5) and (3,4), respectively.

The Fe–4N sites have porphyrin-like configurations, where the Fe atom is coordinated to four N atoms, incorporated in pyridine (py) six-membered or pyrrole (pr) five-membered rings, shown in Fig. 1(d,g) and (e,h), respectively. These structures are obtained by substitution of six carbon atoms by four N atoms and one Fe atom. Since CNTs have an axial symmetry, there are twice as many configurations as in the planar graphene. We call a Fe–4N configuration axial (AX), if one of the axes containing the nitrogen atoms *trans* to the Fe atom is parallel to the CNT axis (Fig. 1(d and e)), and helical (HE) otherwise (Fig. 1(g and h)).

3.2. Nitrogen substitution energies

We compare the stability of different configurations in the N-substituted carbon clusters, and calculate the N-substitution energies using

$$\Delta E_{xN} = E_{site+xN} + yE_C - (E_{site} + \frac{x}{2}E_{N_2}). \quad (1)$$

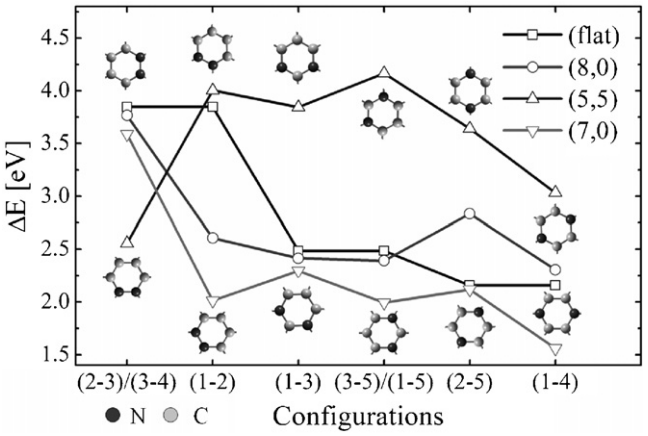

Fig. 2. Nitrogen substitution energies ΔE_{2N} Eq. (1) for the graphene and CNT clusters. On the horizontal axis, the configurations of the two N substitutions are shown for the zigzag/armchair nanotube clusters, as schematically represented by the six-membered carbon rings on the top (bottom) of the graph for the armchair (zigzag) nanotube clusters. The symmetry axis of the CNTs is oriented horizontally. In the flat graphene, the N configurations are double degenerate.

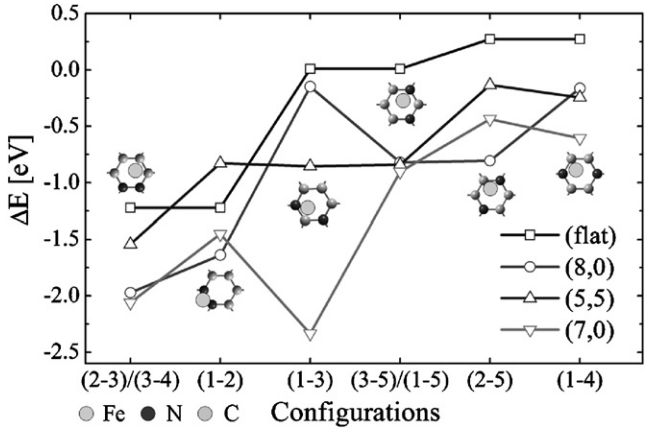

Fig. 3. Fe binding energies ΔE_{Fe} for the planar and curved clusters containing 2 N atoms. The structures are shown schematically on the graph by the six-membered carbon rings and the CNT axis is oriented horizontally.

where, E_C is the total energy of the nanotube per carbon atom, $E_{site+xN}$ and E_{site} are the energies of the cluster with and without the N-substitutions, respectively. The E_{N_2} term is the energy of an isolated N_2 molecule and x stands for the number of N atoms substituting y carbon atoms. The values of x (y) are equal to 2 (2) and to 4 (6) in case of two nitrogen atoms and pyridine (pyrrole) coordination, respectively.

In Fig. 2, we summarize the N-substitution energies for carbon clusters with different configurations. We find that in all cases ΔE_{2N} is positive, indicating that N-doped structures are less stable than pure C structures. For zigzag nanotubes, CNTs with smaller radii have lower lower substitution energies. This is because the total energy per C atom (E_C) is lower for higher CNT curvature. The higher degree of pyramidalization in nanotubes with smaller radius is also more favorable for N incorporation. Comparing our N substitution energies with previous GGA calculations [89], we note that while the nearest-neighbor nitrogen substitutions are energetically preferred for armchair (5,5) nanotube, the increase in the N–N distance lowers the substitution energy for zigzag nanotubes. We also find that planar graphene exhibits substitution behavior similar to zigzag nanotubes. These N-doped structures are local minima and their energies are further lowered by the addition of metal atoms [63], which supports the experimental observation on Fe incorporation in N-doped nanotubes [90].

The results obtained from Eq. (1) for four N atom substitutions are summarized in Table 1. From the ΔE_{4N} values, we can see that a release of spatial strain in zigzag CNTs might be facilitated in the axial rather than helical configurations, which typically have lower ΔE_{4N}. In armchair CNTs, the situation is exactly opposite. The origin of this behavior is in the inequivalent sides of the rectangle formed by four nitrogen atoms because of the difference in their second neighbor shells. This 4N atom configuration in armchair CNTs is quite distinct from the square-planar structures in porphyrins and phthalocyanines. In the (5,5) CNT cluster, the longest side of the N rectangle is perpendicular to the tube axis. The orientation of the N rectangles in the (7,0) and (8,0) clusters is opposite. Nitrogen substitution in the latter orientation is energetically less demanding. This results in a noticeably larger ΔE_{4N}, as seen in the first row of Table 1.

We also compare the two different types of N substitution. The pyrrole-like configurations show the same trend in substitution energies as pyridine-like configurations, but in the higher energy range. The reason why the pyridine-like coordination is preferred over the pyrrole-like one is likely associated with the strain on the surrounding structure exerted by the 5- and 7-membered carbon rings around each nitrogen in pyrrole configuration, as seen in Table 1(top).

Table 1
(top) Nitrogen substitution energies ΔE_{4N}, Fe binding energies ΔE_{Fe} (eV), and Fe–N bond lengths (Å) for the graphene and CNT clusters. The cluster curvature increases from left to right. Pyridine and pyrrole-like coordination sites are denoted as py and pr, respectively

Config.	(flat)	(8,0)	(5,5)	(7,0)
ΔE_{4N}/ ΔE_{Fe}				
AX(py)	5.47/−7.39	3.90/−5.77	5.59/−6.08	3.96/−5.44
HE(py)	5.47/−7.39	4.57/−5.98	4.73/−6.60	5.40/−6.45
AX(pr)	10.79/−8.57	7.85/−8.33	8.67/−7.83	7.34/−8.34
HE(pr)	10.79/−8.57	8.11/−6.69	8.90/−6.27	8.45/−6.57
Fe–4N				
AX(py)	1.87, 1.88	1.97, 1.98	1.87, 1.87	2.00, 2.00
HE(py)	1.87, 1.88	1.91, 1.92	1.93, 1.96	1.86, 1.91
AX(pr)	1.90, 1.92	1.87, 1.87	1.94, 1.94	1.87, 1.90
HE(pr)	1.90, 1.92	1.87, 2.03	1.81, 2.02	1.87, 2.07

3.3. Iron binding energies

Iron atom incorporation is considered here for all calculated x N sites. In the case of two nitrogen atoms, Fe is bound in the vicinity of two N atoms (Fig. 1(a–c)). In porphyrin-like structures, Fe atom is integrated into the plane of the site and coordinated by each of the four N atoms, as shown in Fig. 1(d–h). The results are reported for quintet and triplet spin states of the CNT cluster models containing Fe–2N and Fe–4N, respectively. Our calculations with different multiplicities identify these as the ground electronic states.

We evaluate the stability of the Fe-xN sites through the binding energy of the Fe atom to the N-substituted support using the expression

$$\Delta E_{Fe} = E_{site+Fe} - (E_{site} + E_{Fe}), \quad (2)$$

where E_{Fe} is the energy of an isolated Fe atom. The $E_{site+Fe}$ and E_{site} are the energies of clusters with and without Fe, respectively. The relative stability of the formed sites is also seen from the Fe substitution energy, defined as $\Delta E_{\text{Fe-xN}} = \Delta E_{xN} + \Delta E_{Fe}$, where x is 2 or 4.

In Fig. 3, we compare the binding energies of Fe to a flat graphene and curved CNT surfaces (ΔE_{Fe}) with two-nitrogen substitution. The flat clusters turn out to be the least stable. The binding energies increase as the curvature of the zigzag CNTs increases in the (2-3), (1-3), (3-5) and (1-4) configurations. The configurations of the arm-

chair clusters have higher binding energies ranging from –1.54 eV to –0.13 eV, possibly because of the lower stability of their respective 2N configurations, as shown in Fig. 2. Overall, the sites with neighboring or next neighboring nitrogen atoms are more stable in the presence of Fe atom. The moderately favorable (1-3) configuration of nitrogen atoms is greatly stabilized by the binding of Fe in the (7,0) nanotube cluster (compare Figs. 2 and 3) and has a binding energy ΔE_{Fe} of –2.34 eV. In this configuration, the Fe atom is embedded into the surface of the cluster, in contrast to the other Fe–2N configurations, where the Fe atom primarily resides on top of the N atoms. The distance from Fe atom to the surface of the (7,0) cluster is 1.12 Å and about 1.54–1.95 Å in (1-3) and the other configurations, respectively. The high curvature of the (7,0) nanotube cluster and the position of the nitrogen atoms allows Fe atom to break two C–N bonds and form four new bonds with Fe [65]. However, such stabilization is highly sensitive to the curvature and relative positions of the nitrogen atoms, so it is manifested only for the CNT with the smallest studied radius and results in –0.13 eV and –0.85 eV for (8,0) and (5,5) CNT clusters, respectively.

In Table 1, we show the Fe binding energies for the pyridine- and pyrrole-like Fe–4N catalytic sites. The curvature dependence of the axial py-sites in zigzag nanotubes (Fig. 1(d)) is manifested through a slight decrease of the binding energy from flat to (7,0) clusters. On the contrary, HE(py) sites (Fig. 1(g)) do not show such a decrease in stability with the increasing curvature. This difference between the HE and AX configurations is associated with the orientation of five-membered C_2N_2Fe rings relative to the nanotube axis; the Fe–N bonds in helical configurations are also shorter [65]. These results show that Fe adsorption is strongly dependent on the CNT curvature for small radii. The relative stability of the formed sites is also seen from $\Delta E_{\text{Fe-4N}} = \Delta E_{4N} + \Delta E_{Fe}$ [65]. Overall, the py sites have greater stability than the pr sites, as shown in Table 1. This larger stability might be supported by the observation of pyridinic nitrogen atoms in nitrogenated carbon supports[43,91]. Pyridinic compounds represent very stable fraction and were associated with the most active catalytic sites [43].

3.4. Optimized geometries of the Fe-xN clusters

We have also calculated the optimized Fe–N bond lengths in the flat, bent (8,0), (5,5) and (7,0) cluster models [65]. The calculations show that in Fe–2N the nitrogen atoms are displaced out of the carbon surface by 0.23–0.57 Å. The elevation of the Fe atom above the CNT surface varies in the range of 1.12–2.0 Å. If the two nitrogen atoms are farther apart, the Fe coordinates only to one of them, as in the configuration (1-3) in the (5,5) and (8,0) CNTs. However, in these cases Fe is also bound to one or more C atoms of the nanotube, resulting in longer distances between the second N and Fe. In these structures, the Fe coordination can vary from two N to one N and two C atoms. Further increase of the N–N separation leads to a poor Fe–N-coordination and related inability to form N–Fe–N bridges. This effect is manifested in the (1-4), (2-5) and (3-5) structures [65]. In most cases, the Fe and N atoms are displaced outwards, as a result of the Fe–N bond relaxation. These displacements depend on the Fe-coordination, positions of N atoms and cluster curvature. Very large curvature could compensate for the large N–N distances and decrease the displacement of the Fe atom above the CNT cluster surface, as seen in the (1-3) configuration of (7,0) CNT [65].

The first and second atomic shells in Fe–4N configurations are the same as those in porphyrins, which have four equivalent Fe–N bonds and D_{4h}symmetry. The embedded Fe–4N sites also have four nearly equivalent bonds, but the 4N site has a rectangular shape because of the honeycomb lattice and further distortions due to nanotube curvature. The calculated bond lengths are close to 1.98–2.00 Å reported for Fe porphyrins [92]. For example, the N atoms of the AX(py) (8,0) site form a rectangle with Fe atom in its center. The Fe atom is displaced out of the plane by 0.41 Å for AX(py), while in the case of AX(pr) of the same curvature the displacement is only 0.15 Å. Similar displacement trends are observed in the other studied clusters. The out-of-plane displacement of Fe is larger in pyridine than in pyrrole configurations. In addition, AX(pr) sites (Fig. 1(e)) have lower ΔE_{Fe} and, in general, shorter Fe–N bonds than AX(py) sites [65]. In Section 6, we also briefly discuss how the calculated structures match the experimentally obtained data on metal–nitrogen doped CNTs [65].

4. Metal-doped carbon nanocones

In a recent review, Ewels and Glerup have discussed several possible atomic configurations for the nitrogen doping of carbon nanostructures [46]. Zapol et al. also studied the effects of carbon ad-dimers on the electronic structure of CNTs [93]. Geometry optimization using DFT shows that substitutions of C with N atoms in CNTs lead to less than 0.02 Å shifts in the atomic positions [94,46]. Nitrogen atoms bonded to two and three C atoms in CNT have also been observed experimentally [47]. These authors also show by *ab initio* calculations that N atoms bonded to two C atoms form three stable pyridine-like substitution sites and vacancies in the walls of CNT. Here, we review our theoretical study [63], where we have shown how one can functionalize nitrogen-doping sites and vacancies in carbon nanocones with transition metal atoms.

4.1. Design of metal-doped nanocones

In Fig. 4, we present a series of Ni(II) and nitrogen-doped carbon nanocones that are calculated using DFT/B3LYP/6-311G*The structures have been obtained by stepwise modifications of metalloporphyrins, leading to carbon nanocones with integrated metal binding sites. In analogy to elementary cells in carbon nanotubes (CNTs), we can introduce layers in such structures: the first is the metal, the second contains the N atoms, the third has the C atoms connected to them and to their next C atom neighbors, etc. We consider the following modifications of metalloporphyrins:

1. The metalloporphyrin **1** can be “frustrated” in the third layer, where we remove the four methine C atoms. As a result, we obtain structure **2** that is buckled, since the methine linkers between its four pyrrole rings are removed. The structure is terminated by an “armchair” rim, allowing it to be closed by another cone or to be connected to the (4,4) CNT, as shown in cone **3**.
2. The porphyrin structure **1** can also be “extended” by completing eight benzene rings fused to four pyrrole rings. This creates the flat structure **4**.
3. In nanocone **5**, we close the fourth layer of structure **4**, by adding four more C atoms. The obtained structure buckles, but the resulting tension is relatively small. The cone gains a “zig-zag” rim, fitting the (12,0) nanotube.
4. We can also combine the frustration and extension of the metalloporphyrin **1**, as shown in the cone **6**, where the methine linkers are removed and the five-membered pyrrole rings are substituted with six-membered pyridine rings. Structure **6** is fully based on the 120° carbon nanocone [7,95] and differs from it in *four* N–C substitutions, and a closure with a Ni atom instead of *two* C atoms.
5. In order to modify a 180° carbon nanocone, such as **7**, the metalloporphyrin is frustrated by a pyrrole defect, as shown in cones **8** and **9**. Cone **9** differs from **7** in *three* N–C substitutions and closure with a Ni atom instead of *one* C atom. Cones **8** and **9** are analogous in structure to cones **5** and **6**, respectively. Cones **5** and **8** contain pyrrole N atoms, whereas cones **6** and **9** contain pyridine N atoms. However, cones **8** and **9** are sharper than cones **5** and **6**,

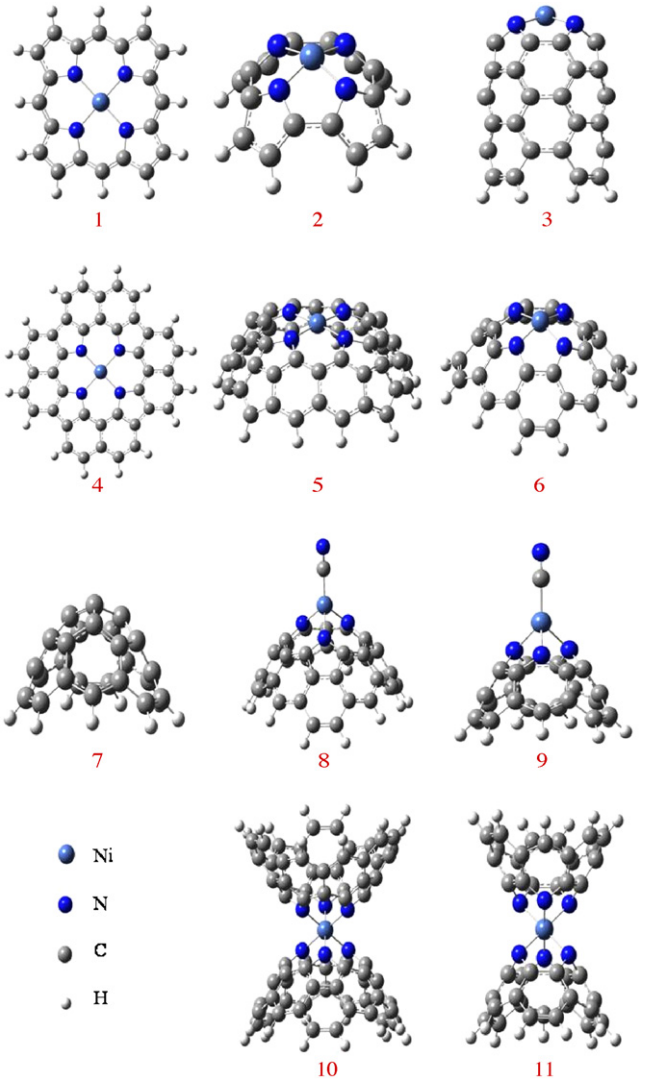

Fig. 4. Carbon nanocones doped with Ni(II) and N atoms. Structures **1**–**6** are in the first group whereas **7** –**11** are in the second group.

and form tetrahedral as well as octahedral complexes. The tetrahedral complexes **8** and **9** are completed here by cyanide ligands. The octahedral complexes **10** and **11** are formed by the binding of two cones to one metal atom.

All these metallo-capped cones can be continued by adding more C atom rings, in such a way that they follow the structure of typical carbon nanocones [7]. Moreover, their rims could be arranged to fit either zig-zag or armchair tips of nanotubes, depending on the layer where we perform their frustration.

We use Ni(II) because it forms stable square planar, tetrahedral and octahedral complexes. We treat the complexes shown in Fig. 4 as neutral, in analogy to Ni(II)porphyrin. They can be divided into two groups, depending on the number of coordinating N atoms of the nanocone ligand (NL). The square planar complexes **1** –**6** that contain tetradentate NLs comprise the first group. Complexes **8** –**11** that contain tridentate NLs are in the second group. The four-coordinate complexes **8** and **9** contain one tridentate NL and one cyanide ligand, while the octahedral complexes **10** and **11** contain two identical tridentate NLs.

We study separately the NLs. The tetradentate ligands of cones **1** –**6** are optimized as dianions, whereas the tridentate ligands in complexes **8** –**11** are optimized as monoanions. We also perform

Table 2
Selected optimized N–N distances for anionic ligands (N–N(L)) and for cones (N–N(co)), Ni–N distances (Å), N–Ni–N angles (°), Mulliken Ni atom charges (q(Ni), *e*), Ni–N(ligand) total binding energies ($E_b(co)$, eV), and HOMO–LUMO gaps (H–L, eV) for the cones in their ground electronic states (GS). The GS *s*, *d*, *t*, *qr* and *qn* are singlet, doublet, triplet, quartet and quintet, respectively. The HOMO–LUMO gaps of open-shell systems are determined relative to LUMOs of the same spin type as the HOMOs. The N–N distances for **1** –**6** are for N atoms *trans* to the Ni atom. The N–N distances for **8** –**11** are for N atoms that belong to the same tridentate ligand. The N–N distances for ligands are defined as in the corresponding cones. The N–Ni–N angles for **8** –**11** involve N atoms that belong to the same ligand.

Cone	GS	N–N(co)	N–N(L)	Ni–N	N–Ni–N	q(Ni)	$E_b(co)$	H–L
1	*s*	3.94	4.17	1.97	90.0	1.08	−12.00	3.12
2	*s*	3.56	3.75	1.83	87.1	0.97	−11.61	2.35
3	*s*	3.74	3.99	1.92	87.5	0.64	−9.21	1.86
4	*t*	3.91	4.09	1.96	90.0	1.11	−12.14	3.03
5	*s*	4.00	4.39	2.00	89.8	1.08	−10.87	0.95
6	*s*	3.57	3.68	1.83	87.5	1.03	−7.72	1.20
7	*d*	–	–	–	–	–	–	1.71
8	*qn*	2.69	2.68	1.97	86.2	1.27	−12.52	1.17
9	*qr*	2.52	2.55	1.97	80.2	1.21	−11.09	2.05
10	*t*	2.63	2.68	1.88	90.5	1.33	−13.70	0.94
11	*s*	2.57	2.55	1.89	86.1	1.21	−10.38	1.83

geometry optimization of all NLs as neutral molecules. Both the dianionic and the neutral NLs of cones **2**, **5** and **6** have cup shapes that resemble calixarenes. We use the results for the analysis of the geometrical changes caused by the metal coordination and for the calculation of the heterolytic and homolytic binding energies.

4.2. Ground states of metal-doped nanocones

For all complexes and NLs with even number of electrons, we determine the ground electronic state among the closed-shell singlet, open-shell singlet, triplet and quintet states. For systems with odd number of electrons, such as **7**, **9** the anionic NL of **11** and the neutral NL of **10**, the ground electronic state is either the open-shell doublet or quartet state.

For the first group of complexes, the results listed in Table 2 show that **1** –**3**, **5** and **6** have closed-shell singlet ground states, whereas **4** has an open-shell triplet ground state. The closed-shell singlet ground state of **1** is in agreement with the experimental observations [96]. The open-shell triplet state energies of complexes **1**, **2** and **3** are 1.3, 1.1 and 0.2 eV higher than the respective closed-shell singlet ground state energies. However, for **4** –**6** the differences between the lowest-lying triplet and singlet states are only about 0.05 eV.

In the second group, the four-coordinate complexes **8** and **9** have open-shell quintet and quartet ground states, respectively. The quartet ground state of cone **9** arises from the odd number of electrons in the neutral complex. Similarly, the pure carbon cone **7** has odd number of electrons and a doublet ground state. The octahedral complexes **10** and **11** have open-shell triplet and closed-shell singlet ground states, respectively. The ground state energies of complexes **8** –**11** are at least 0.1 eV lower than the lowest-lying states of different multiplicity.

We also evaluate the spin purity of these ground electronic states, determined by the percent spin contamination $\langle \Delta S^2 \rangle_{cont}$, given by the following expression:

$$\langle \Delta S^2 \rangle_{cont} = [\langle S^2 \rangle - S(S+1)]100/[S(S+1)]. \quad (3)$$

The $\langle S^2 \rangle$ values are obtained as part of the geometry optimization output, while the $S(S+1)$ values are 0.75, 2.00, 3.75 and 6.00 for doublet, triplet, quartet and quintet spin states, respectively. The percent spin contamination is considered acceptable when it is less than 10% [97]. For the triplet ground states of complexes **4** and **10**, the values of the spin contamination are 0.5% and 5%, respectively. The doublet pure carbon cone **7** has a spin contamination of 5%.

The spin contamination is 1% for each of the quartet **9** and quintet **8** cones. These results show that the ground state spin multiplicities listed in Table 2 are rather pure.

The anionic NLs ground states affect the ground states of the corresponding complexes. The anionic ligands of **1** –**3** and **6** have closed-shell singlet ground states, whereas these of **4**, **5** and **10** have open-shell triplet ground states. Thus, the large anionic NLs of **4** and **10** form high spin complexes. The anionic NL of **11** has an odd number of electrons and an open-shell doublet ground state. The neutral NLs are optimized in closed-shell singlet state for **1** –**6** and **10**, and in open-shell doublet state for **11**. The different ground electronic states and the energetic closeness of states with different multiplicity could make these structures useful for magnetic applications.

The energy gaps between the highest occupied molecular orbital (HOMO) and the lowest unoccupied molecular orbital (LUMO) of the complexes, listed in Table 2, depend strongly on the character of the ground state. The dianionic ligands of **4** and **5** that have triplet ground states, have the largest energy gaps. The energy gaps of our structures decrease as the size of the conjugated π-system size increases, similar to the conjugated porphyrin tapes [60]. Also, the energy gaps decrease as the buckling angle increases. These two effects are demonstrated by the decreasing energy gaps of the complexes from **1** to **2**, due to buckling, and from **2** to **3**, due to enlargement of the π-system. Similarly, for complexes **8** –**11**, the structures containing the larger cone have smaller energy gaps. The HOMO–LUMO gaps of the doublet carbon cone **7** and the structurally similar ligand of complex **9** differ by only 0.18 eV.

4.3. Optimized geometries of metal-doped nanocones

In Table 2, we list selected structural parameters obtained from the ground state geometry optimization of the complexes shown in Fig. 4 and the related anionic NLs. The NLs with extended π-structures are relatively rigid and undergo small geometrical changes upon metal coordination, mostly observable at the N atom positions. These changes can be quantitatively evaluated from the relative changes in the N–N distance *trans* to the Ni atom. For our reference metalloporphyrin system **1**, this N–N distance decreases from 4.17 Å for the ligand to 3.94 Å for the complex, i.e. by 5.5%. Larger relative changes of 6.3 and 8.9% occur only for cones **3** and **5**, respectively. The tridentate NLs undergo even smaller relative changes than the tetradentate NLs.

We also study the Ni–N distances and N–Ni–N angles, connecting neighboring N atoms, in these complexes and present the results in Table 2.In the first group of complexes, we can find large structural variations. Complexes **1** and **4** are planar, as shown by the N–Ni–N angle of 90°, and have Ni–N distances of 1.97 and 1.96 Å, respectively. The Ni–N distance and N–Ni–N angle for the Ni(II)porphyrin **1** have been determined at 1.95 Å and 90.0°, respectively, using X-ray crystallography [98]. The calculated N–Ni–N angle of **1** is in excellent agreement with the experimental value, whereas the calculated Ni–N distance is 0.02 Å longer than the experimental one. In complex **5**, the Ni atom lies approximately in the plane of the four N atoms, similar to complexes **1** and **4**. This makes complex **5** almost square planar, although its NL is bowl-shaped. Despite the fact that the N-N distance of **5** undergoes the largest relative shortening upon complexation, the Ni–N distance of 2.00 Å in complex **5** is still the longest.

In complex **2**, the removal of the four methine linkers causes large buckling, reflected in the N–Ni–N angle of 87.1° and the shortest Ni–N bond of 1.83 Å. In cone **3**, the two unit cells of (4,4) CNT form a rigid carbon π-system that deforms the tetrapyrrole cap and causes an increase of the *trans* N-N distance relative to **2**. This deformation results in the Ni–N bond elongation of 0.09 Å in **3** relative to **2**, while the degree of buckling in these two structures is the same. In complex **6**, both the N–Ni–N angle and the Ni–N distance are similar to **2**. The buckling effect in complexes **2**, **3** and **6** represents a displacement of the metal atom above the NNNN plane and a pyramidal distortion of the square planar complex.

This distortion breaks the square planar symmetry and allows for axial binding of a fifth ligand to the metal atom and the formation of a square pyramidal complex. The axial ligand binding is favored because the complex is already "pre-bent". This effect is similar to the "pre-bending" proposed for the synthesis of bucky-bowls [99]. In our buckled complexes, the smaller the value of the N–Ni–N angle is, the easier it is to bind another ligand. A convenient way to decrease this angle is to coordinate a larger transition metal ion. For example, the substitution of Ni(II) for Ru(II) in cone **2** causes a decrease of the buckling angle to 77.5°. Thus, cones **2** and **3** with Ru(II) on the tip have the potential to coordinate bidentate ligands, such as 2,2'-bipyridine [63].

In the second group of complexes, the Ni–N bonds in the four-coordinate **8** and **9** are as long as those in the Ni(II)porphyrin. The N–Ni–N angles of **8** and **9** are smaller than 109.3° for a regular tetrahedron because of the rigid tridentate NLs. These four-coordinate complexes are functionalized with cyanide ligands. The substitution of other strong-field ligands for cyanide represents a feasible pathway for functionalization. On the other hand, our attempts to optimize four-coordinate complexes containing weaker-field ligands, such as chloride, ammonia and water, instead of cyanide have produced unstable species. This is because the strong ligand field provided by the electron-rich nitrogen-doped NLs generally favors the binding of another strong-field ligand, such as cyanide, rather than a weaker-field ligand [53].

The octahedral complexes **10** and **11** feature the Ni–N distances of 1.88 and 1.89 Å, respectively. The N–Ni–N angles are close to 90°, as expected for the octahedral geometry. The spatial arrangement of the coordinating N atoms in the octahedral complexes **10** and **11** is structurally similar to the triazacycloalkane Ni(II) complexes [100], but the N–Ni–N angle of 86.1° for complex **11** shows a smaller distortion from the octahedral symmetry than in $[Ni(1,4,7\text{-triazacyclononane})_2]^{2+}$ having the angle of 82°. Therefore, the optimized geometries of the two octahedral complexes with two NLs have low steric strain. Ligand substitution in these complexes is not favorable because the chelate effect of the tridentate NLs strengthens the Ni–NL bond. Cone **7** is structurally analogous to cone **9** where the cyanide ligand is removed.

In Table 2, we also show the Ni atom charges. They increase from the first to the second group of complexes. Within the first group of complexes, the charges slightly decrease along the rows in Fig. 4, from the flat **1** and **4** to the buckled **3** and **6**, respectively. This decrease of the Ni atom charge correlates with the decrease of both the N–Ni–N angle and the NL size, seen in Fig. 4. In complex **2**, the Ni charge decreases by 0.17 relative to the Ni(II)porphyrin **1**, as we reduce the ligand size and introduce buckling. In complex **3**, the Ni charge increases by 0.09 relative to **2**, as we increase the NL size. These results could help to determine which NLs form cones that are more convenient for functionalization. Since higher metal atom charges lead to the formation of stronger axial bonds, complexes with larger NLs might be better candidates. This effect shows that the conjugated system acts as an electron sink. Of the complexes in the first group, the planar complex **4** seems to be best for functionalization.

In the second group of complexes, the Ni atomic charges also increase as the conjugated carbon systems increase in size. This can be seen when comparing **9** and **11**, which contain a smaller cone, to **8** and **10**, respectively, which contain a larger cone. In cone **7**, the natural charge at the cone tip carbon atom, which represents the first layer, is +0.12 e, while atoms of the second, third and fourth layers have charges of −0.06, +0.01 and −0.06 e, respectively.

4.4. Metal-ligand binding energies in nanocones

The metal-ligand bond dissociation energies are crucial for the stability of all the complexes. We calculate these energies for homolytic ($E_b(co)$) dissociation yielding neutral metal and ligand.

$$E_b(co) = E(\mathrm{n}) - E(\mathrm{L}) - E(\mathrm{Ni}) - E(\mathrm{CN}). \quad (4)$$

Here, E(n), E(L) and E(Ni) are the total energies of a cone n, neutral ligand(s) and a singlet Ni atom, respectively. E(CN) (nonzero for cones **8** and **9**) is the energy of doublet CN^0. These energies are obtained for the optimized geometries of the structures and include the energy changes arising from the changes in geometry that occur as a result of the bonding.

From Table 2, we found that the bond dissociation energy of the Ni(II)porphyrin calculated using the B3LYP/6-311G*in Gaussian 03 is 1.9 eV higher than the value reported using the TZP basis set in the ADF software package [58]. We get a difference of 10-20% between these two approaches also for the other cones. Here, we focus on the relative changes in the binding energy that reflect the changes in their structure.

For the first group of cones, $E_b(co)$ decreases along the rows of Fig. 4, showing weaker M-L bonds for the buckled complexes, relative to the planar complexes. For complex **6**, we obtain a relatively low $E_b(co)$, due to a different degree of electronic structure stabilization upon homolytic binding. The neutral ligand of **6** has the lowest-lying HOMO and the dianionic ligand has the highest-lying HOMO energy, relative to the rest of the first group ligands. The buckled structures with weaker M-L binding have higher potential towards binding of a fifth ligand.

For the second group of complexes, the $E_b(co)$ values in **8** and **10** are higher than in **9** and **11**, respectively, because the tridentate ligand in the first pair provides larger N–Ni–N angles. The largest value of $E_b(co)$ is obtained for complex **10** that has N–Ni–N angle of 90°, as required for the octahedral geometry. The heterolytic bond dissociation energies of the octahedral complexes are higher than in the four-coordinate ones because of the more efficient bonding.

4.5. Stability of metal-doped nanocones

The results above show that the complexes of the second group do not possess significant steric strain. Therefore, we will discuss the cone **2** in the first group, which is probably the least stable. Here, the steric strain caused by the buckling is the strongest, since the methine linkers are removed and stabilization by the extended conjugated system is also absent. To understand the stability of this complex, we address first the aromaticity of its dianionic ligand, shown in Fig. 5.

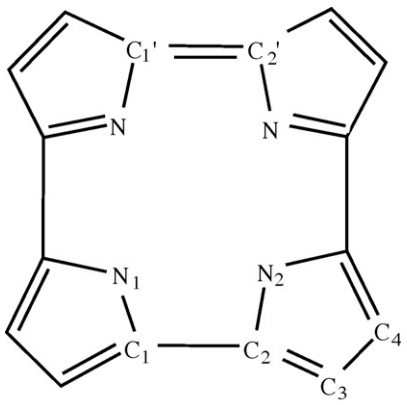

Fig. 5. Diagram of the dianionic ligand of complex **2**.

In Fig. 5, we have 18π-electrons presented by the 9 π-bonds and 4 π-electrons from the lone pairs of the N_1 and N_2 atoms, or a total of 22 π-electrons. The π-electron count shows that the ligand is aromatic, as it fulfills the $4n$ +2 rule, where n is a positive integer. The optimized structure of the ligand is buckled with a conformation similar to complex **2** from Fig. 4. Buckled aromatic compounds have a high degree of strain, due to the pyramidalization of the sp^2 carbon atoms. The experimental preparation of such structures is a synthetic challenge. Recently, several experimental approaches have been successfully developed for the synthesis of highly strained buckled aromatic compounds as precursors of fullerenes and other nanostructures [99].

We first evaluate the bond orders for the C_1–C_2 and C_3–C_4 bonds. Our geometry optimization results show that the four pyrrole-pyrrole bonds in Fig. 5 are equivalent for both the ligand and the complex **2**. As shown in Fig. 5, the dianionic ligand of complex **2** contains one double bond (C_1'–C_2') and three single bonds, or a total of five bonds distributed over the four pyrrole-pyrrole distances. This makes a formal bond order of 5/4 = 1.25. This formal bond order is in a very good agreement with the calculated Wiberg bond orders of 1.23 and 1.19 for complex **2** and its dianionic ligand, respectively. The formal C_3–C_4 bond order of 1.50 is also in relatively good agreement with the calculated values of 1.59 and 1.61 for the complex and the ligand, respectively.

From Fig. 4, it is obvious that the stability of the ligand of complex **2** is contingent upon the strength of the pyrrole–pyrrole bond C_1–C_2. We calculate the homolytic cleavage energy of this bond as the difference between the energy of the neutral singlet ligand of **2** and the energy of the neutral linear tetrapyrrole in its triplet ground state. The value of –3.6 eV obtained shows that the cyclic ligand is stable. This ligand might be further stabilized by additional groups. In fact, the functionalization of the open CNT might be a feasible way of experimental preparation. A natural way how to stabilize this structure is by the addition of (4,4) CNT unit cells, as shown in **3**. We can expect that the other complexes in Fig. 4 are more stable than **2** because of the presence of extended π-aromatic structures.

4.6. Axial coordination of ligands to metal-doped nanocones

For the complexes of the first group, the deviation of the N–Ni–N angle from 90° is a measure of the pyramidal distortion from the square planar geometry. This distortion breaks the plane of symmetry and makes the transition metal coordinationally unsaturated, allowing it to bind different types of ligands. Thus, the buckled structures shown in Fig. 4 have two different binding sites with different geometrical and electronic environment.

As we show in Fig. 6, the buckling of the structure leads to an asymmetric distribution of the Ni *4s* and *3d* orbital lobes relative to a plane of symmetry that contains the Ni atom and is parallel to the NNNN plane. The different sizes of the metal orbital lobes mean different electronic environment for ligands approaching from the top and from the bottom. Consequently, in principle cones **2**, **5** and **6** can bind two axial ligands with different strength—one above and the other below. In complex **5**, the two ligand binding sites have similar electronic structure but different geometries, because the bowl-shaped ligand does not allow equivalent binding of large ligands above and below this structure. The planar complexes **1** and **4** provide two equivalent binding sites. Cone **3** binds only one ligand on top. We selected this cone for the electric field study presented in the last section.

In order to show the different axial binding modes, we optimize the geometries of dianionic complexes **2**, **5** and **6** that contain two cyanide ligands coordinated at the two axial positions. The Ni–C bond lengths for cyanide ligands coordinated axially at the top and at the bottom of these complexes are (Ni–C_t) and (Ni–C_b), respectively. For complex **2**, we obtained a Ni–C_t bond length of 1.92 Å,

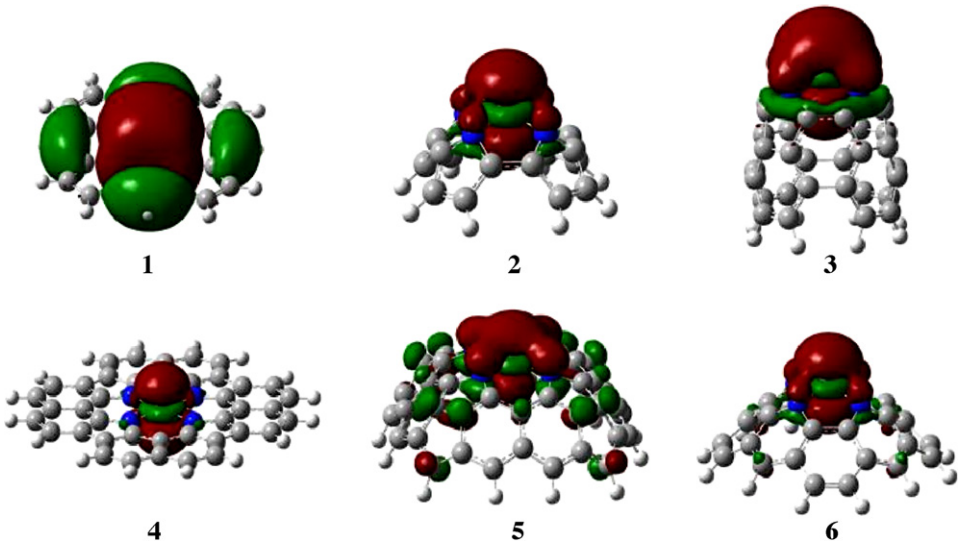

Fig. 6. Schematic diagrams of the molecular orbitals that contain major Ni d_{z2} and *s* atomic orbital contributions for the cones of the first group.

which is shorter than the Ni–C_b bond length of 2.01 Å. For complexes **5** and **6** we found the opposite, namely that the Ni–C_t bond lengths of 1.95 and 1.89 Å are longer than the respective Ni–C_b bond lengths of 1.90 and 1.86 Å. These axial binding results show that nanocones with large π-systems form weaker bonds with π-ligands at the cone tip than inside the cone. Also, the axial ligand binding to cones with larger NL sizes (**5**) is stronger than to cones with smaller NL (**6**).

5. Metal-doped carbon nanocapsules

Carbon nanocapsules doped by metals and functionalized by ligands might have many interesting applications. In this Section, we review our recent theoretical studies of metal-doped nanocapsules [64].

We could build a "periodic table" of doped nanocapsules. One can start from the smallest observed fullerene, C_{20}, which contains 12 pentagonal rings and is highly strained because of the extreme pyramidalization of its double bonds. Its stability arising from electron correlations [101] might be controlled by doping, as shown by Alder et al. [102]. The $C_{12}P_8$fullerene can be particularly stable, whereas $C_{12}N_8$should be very unstable. Pattanayak et al. [103] investigated BN-doping of small (C_{20}–C_{40}) fullerenes and found that the BN pair would preferably replace a short C–C bond located at the hexagon-pentagon junction, due to the polarization of the system. A number of metal-doped analogs of C_{20}, called metalcarbahedrenes (met-cars) that contain 8 Ti, V or Mo atoms have also been synthesized by Castleman group and others [104–107]. In particular, $Ti_8C_{12}^+$is a promising catalyst for hydrodesulfurization of oils, because of its strong interaction with thiophene [108]. Theoretical predictions show that C_{20}has a remarkable activity towards the addition of alkenes [107], while $C_{36}$is highly reactive and has a strong tendency to form intermolecular covalent bonds. The applications of fullerenes in electronics have been also explored. $C_{20}$and C_{36} have been encapsulated in semiconducting CNTs [109], leading to various peapod structures. Highly stable and the most studied fullerene [12] C_{60} can be chemically activated upon introduction of heteroatoms, such as Si [110], B and N [111–114]. The insertion of different types of metallofullerenes into CNTs, such as Gd encapsulated in C_{82}[115], could allow for their complex band-gap engineering [116].

Here, we describe carbon fullerenes that contain several embedded porphyrin-like moieties [64], optimized using the B3LYP exchange-correlation functional [68]. For the main-group and the first-row transition metal atoms, we apply the 6-311G** basis set [75,76]. For the third and fourth row transition metal atoms, we treat the core electrons using the SDD ECP, whereas for the valence electrons we employ the SDD basis set [79,80].

5.1. Design of metal-doped nanocapsules

In Fig. 7, we present the optimized geometries of a series of Ni, N and B-doped nanocapsules that are structurally related to C [1–3] and BN [117] fullerenes, as well as to Ni(II) and N doped carbon nanocones [63]. These polymetallic capsules are obtained as follows:

1. The smallest metallo-capsule **1** is obtained from the I_h isomer of C_{20} in whose tips two pairs of fused 5–5 rings are substituted with two pairs of 4–4 rings. In Fig. 8 (left), we show part of the surface of carbon fullerene C_{20} that contains fused 5–5 rings. In this structure, two adjacent C atoms are substituted with a single Ni atom. Also, all four C atoms adjacent to Ni are substituted with N atoms to yield a NiN_4 moiety that contains 4–4 rings. In capsule **1**, the N atoms are part of four pyrrolic rings. Bimetallic capsule **1** can also be designed from two doubly-fused biimidazole ligands. Its structure is similar to some photochemically active Ru(II) complexes [118]. The 8 N atom substitution mode of C_{20}considered by Alder et al. [102] is the same as in **1**.
2. Nanocapsule **2** is obtained from the D_{2d} isomer of C_{36}, where two pairs of fused 6–6 rings are substituted with two pairs of 5–5 rings. In Fig. 8(right), we show a part of the C_{36} fullerene surface that contains fused 6–6 rings. In this structure, two adjacent C atoms at the 6–6 ring fusion area are substituted with a single Ni atom. Also, all four C atoms adjacent to Ni are substituted with N atoms to yield a NiN_4 moiety that contains 5–5 rings. In capsule **2**, the four N atoms belong to four pyrrolic rings. This capsule can also be designed by fusion of two metal-tipped nanocones [63] and extended by addition of CNT segments. Capsule **3** is obtained by insertion of a (4, 4) CNT unit cell into capsule **2**.
3. Nanocapsule **4** is obtained from the I_h isomer of C_{60}, where two pairs of fused 6–6 rings located at the opposite sides of the buckyball are substituted with two pairs of 5–5 rings (Fig. 8(right)). In capsule **4**, the N atoms belong to pyridinic rings. This structure differs from C_{60} in *eight* C to N substitutions and *two* closures with Ni atoms instead of two C atoms. It can also be designed by fusion of two 120° cones [7,95] along the "zig-zag" rim [63].

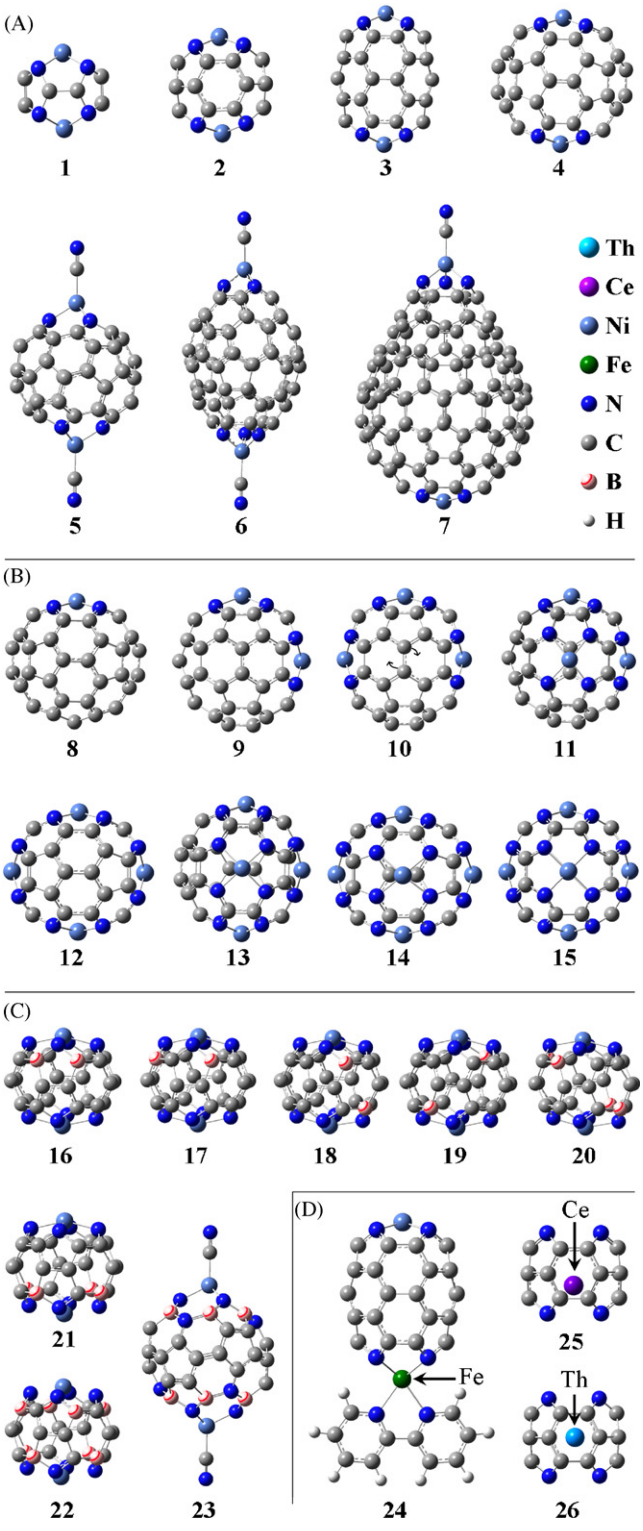

Fig. 7. Metal-doped carbon nanocapsules.

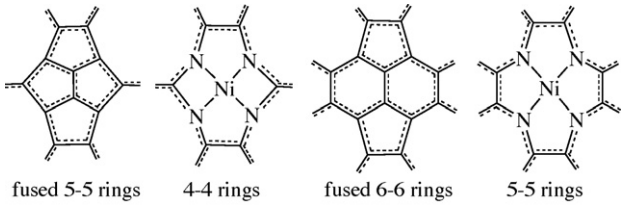

Fig. 8. Metal and nitrogen doping patterns for capsules **1** (left) and **2** –**4** (right).

4. Nanocapsule **5** is obtained from a 180° cone frustrated by three pyrrole defects. The all-carbon analog of capsule **5**, C_{56} would be highly strained, due to two pairs of fused 6-membered rings that share one C atom. Nanocapsule **6** is also obtained from a 180° cone, and it is analogous to the D_3 isomer of C_{68} [111]. Capsules **5** and **6** contain two Ni atoms that form four-coordinate (approximate tetrahedral) complexes. The tetrahedral coordination is completed by the additon of a CN^- ligand. Metal-doped 180° cones can also form octahedral complexes [63].
5. Nanocapsule **7** is obtained from 180° (top) and 120° bottom cones [7,95] fused as in (12,0) CNT. The top portion differs from the carbon 180° cone in three N–C substitutions and a Ni atom at the tip instead of a C atom. The bottom portion differs from the carbon 120° cone in four N–C substitutions and a Ni atom at the tip instead of two C atoms.
6. Nanocapsules **8** –**15** are obtained from C_{60} and contain 1-6 Ni atom closures, designed in analogy to these in capsule **4**. In addition, we consider the isomer of capsule **10** (listed as **10**') obtained by Stone-Wales rearrangement, as shown by the arrows. The capsules **10**, **10**' and **11** are isoelectronic structural isomers. Capsule pairs **9** and **4** as well as **12** and **13** are also isoelectronic structural isomers.
7. The capsules can be further doped with B atoms, as shown in **16** –**23**. Isoelectronic capsules **16** –**19** are obtained by two B-atom doping of **2**. Isoelectronic capsules **20** and **21** are obtained by four B-atom doping of **2**, whereas capsule **22** is obtained by eight B-atom doping of **2**. Capsule **23** is obtained by twelve B and six N atom doping of **5**.
8. Capsule **24** contains Fe(II) and Ni(II). The octahedral coordination of Fe(II) is completed by the addition of a 2,2'-bipyridine (bpy) ligand.
9. Structures **25** and **26** are Ce(IV) and Th(IV) encapsulated in the ligand of **2**. Cerium is smaller and displaced off the ligand center, whereas larger metal ions, such as U(IV) are too big to get encapsulated in this ligand.

These capsules can be extended by adding larger C atom cones that would elongate them and increase their diameter. One could also insert in them CNT segments that would elongate them. The capsule fusion rims can be designed to have "zig-zag" or "armchair" structures.

We use Ni(II) in the capsule doping, because it forms stable square planar and tetrahedral complexes. We treat the capsules in Fig. 7 as neutral, in analogy to the Ni-doped nanocones [63]. Capsules **1**–**4**, **9** and **16** –**22** contain two Ni atoms and octadentate *capsule ligands* (CLs). Capsules **5**, **6** and **23** contain two Ni atoms and hexadentate CLs. Capsule **7** contains two Ni atoms and a heptadentate CL, whereas capsule **8** contains a tetradentate CL. Capsules **10** –**16** contain from three to six metal atoms and multidentate CLs.

In Fig. 7, we organize these capsules in four structurally dissimilar groups labeled **A**–**D**. In group **A**(Fig. 7(top panel)), we include capsules **1** –**7** that comprise the seven distinct capsule frameworks considered in this article. In group **B** (Fig. 7(middle panel)), we include capsules **8** –**15** that are obtained by Ni-doping of capsule **4**. In group **C** (Fig. 7(bottom panel)), we include capsules **16** –**23** that are obtained by B-doping of capsules **2** and **5**. In the last group **D** (Fig. 7(bottom right panel)), we include capsules **24** –**26** that contain Fe-doping and encapsulated heavy metal ions.

5.2. Ground states of metal-doped nanocapsules

All capsules contain even number of electrons. The CLs also contain even number of electrons, except for the CL of **7**. For structures that contain even number of electrons, we determine the *ground electronic state* as the state with the lowest total energy among the closed-shell singlet and the open-shell triplet, quintet, heptet,

Table 3
Selected optimized metal–N (M–N) and metal-metal (M–M) distances (Å), binding energy ($E_b(ca)$, eV), HOMO–LUMO gaps (H–L, eV) and Mulliken metal atom charges (q, *e*) Mulliken metal atom spin densities (Spin(M), *e*) for the capsules in their ground electronic states (GS). The GS types *s*, *t*, *qn*, *h*, *n* and *ed* are singlet, triplet, quintet, heptet, nonet and endecet, respectively. The HOMO–LUMO gaps of open-shell systems are determined relative to LUMOs of the same spin type as the HOMOs. For capsules **10**, **10'** and **12** –**15**, only the diametral M–M distances are listed.

Capsule	GS	q/Spin(M)	M–N	M–M	$E_b(ca)$	H–L
Group **A**						
1	*qn*	1.17/1.55	1.98	4.24	−5.90	2.61
2	*s*	1.03	1.91	4.88	−8.51	1.55
3	*s*	1.01	1.91	7.32	−8.94	1.09
4	*s*	1.02	1.88	6.71	−7.73	1.00
5	*h*	1.30/1.75	1.95	8.23	−12.40	0.94
6	*qn*	1.22/1.62	1.96	11.31	−11.38	1.15
7 (top)	*t*	1.22/1.64	1.97	13.85	−11.55	1.11
7 (bot.)	*t*	1.02/0.00	1.85	13.85	−9.53	1.11
Group **B**						
8	*s*	1.02	1.89	–	−7.61	1.03
9	*t*	1.00, 1.01/0.02, 0.03	1.88	4.72	−7.56	0.93
10	*s*	1.02	1.89	6.56	−7.79	1.34
10'	*s*	1.01–1.02	1.89–1.90	7.20	−7.59	1.09
11	*t*	1.01–1.02/0.00–0.02	1.87–1.90	4.78–4.80	−7.44	1.05
12	*s*	0.99–1.01	1.89	6.34, 7.06	−7.81	1.85
13	*s*	1.00-1.02	1.88-1.90	6.73	−7.55	1.33
14	*s*	0.99-1.03	1.89	6.51, 6.93	−7.60	1.24
15	*s*	0.98-1.00	1.89	6.70, 6.79	−7.48	1.10
Group **C**						
16 (top)	*t*	1.03/0.02	1.94, 1.95	4.96	−9.41	1.17
16 (bot.)	*t*	1.02/0.01	1.89-1.92	4.96	−9.41	1.17
17 (top)	*s*	1.04	1.91, 1.95	4.90	−9.16	1.56
17 (bot.)	*s*	1.02	1.88-1.91	4.90	−9.16	1.56
18	*s*	1.03	1.92, 1.91	4.91	−9.48	1.54
19	*s*	1.04	1.91, 1.90	4.91	−8.89	1.22
20	*s*	1.03	1.95, 1.92	4.99	−9.24	1.21
21 (top)	*s*	1.03	1.96	5.01	−10.25	1.90
21 (bot.)	*s*	1.01	1.90	5.01	−10.25	1.90
22	*t*	1.02, 1.03/0.10	1.96, 1.92	4.95	−9.99	1.45
23	*ed*	1.31/1.87	1.90	8.27	−13.20	1.18
Group **D**						
24 (Ni)	*qn*	0.99/0.00	1.91	8.01	−8.94	1.16
24 (Fe)	*qn*	1.47/3.78	2.18	8.01	−12.15	1.16
25 (bot.)	*s*	0.05	2.44-2.53	–	−7.92	1.35
26	*s*	0.24	2.81-2.90	–	−9.67	1.57

nonet and endecet states. The ground electronic state of the CL of **7** is determined as the state with the lowest total energy among the open-shell doublet, quartet and sextet states. The ground state search is also aimed at the minimization of the percent spin contamination $\langle \Delta S^2 \rangle_{cont}$ Eq. (3). For triplet, quartet, quintet, heptet, nonet and endecet spin states, the *S* values of 1.00, 1.50, 2.00, 3.00, 4.00 and 5.00 yield $S(S+1)$ values of 2.00, 3.75, 6.00, 12.00, 20.00 and 30.00, respectively. A value of $\langle \Delta S^2 \rangle_{cont}$ that is lower than 10% (0.1) before spin annihilation should indicate that the spin contamination is negligible [97]. In our search of ground states, we apply a stricter criterion of $\langle \Delta S^2 \rangle_{cont} < 2\%$ before spin annihilation.

The results are listed in Table 3. In group **A**, the ground state of the smallest capsule **1** is quintet, whereas the ground states of capsules **2**–**4** are singlet. In these four capsules, the Ni coordination is pseudo square-planar [63]. For comparison, the ground states of pure carbon fullerenes $C_{20}$and C_{60}in the I_h symmetry are singlet [119,120]. The ground state of C_{36}in D_{6h} is triplet [121,122]. The ground states of capsules **5** and **6** are heptet and quintet, respectively. In these capsules, the Ni coordination is pseudo tetrahedral [63]. For comparison, the metal-doped nanocones, related to capsules **5** and **6**, have quintet and quartet ground states, respectively [63]. The ground state of capsule **7**, related to capsules **4** and **6**, is triplet. These results show that the ground state multiplicity of the metal-doped capsules increases as high-spin metal species (i.e. tetrahedral Ni) are introduced. The Ni-doped capsule ground state multiplicities are also higher than the respective cones [63].

In group **B**, the ground states are singlet, except for capsules **9**, **11** and **13** that have triplet ground states. This suggests that metal doping at adjacent sites could produce structures with higher ground state multiplicity. In group **C**, the ground states are singlet, except for capsules **16** and **22** that have triplet ground states. The ground state of capsule **23** is endecet, suggesting that BN doping could be particularly effective for ground state tuning. In group **D**, the ground state of the bimetallic capsule **24** is quintet. Ground states with high multiplicity are typical for Fe(II) complexes, because Fe(II) has small octahedral ligand-field splitting energy. The ground states of capsules **25** and **26** that contain a Th and a Ce atom, respectively, are singlet. These results show that the ground state multiplicity of the metal and B-doped fullerenes depend strongly on the nature and organization of the dopants.

We discuss the stability of metal and boron-doped capsules by comparing their ground state energies. First, we consider the parent structure **4** and the Ni-doped capsules of group **B**. For 2 Ni atom doping, the capsule **9** is more stable than **4** by 0.16 eV. The 3 Ni atom doping is in the three isomers **10**, **10'** and **11**. In capsule **10**, there are 2 Ni doping sites located on both sides of fused 6–6 rings, whereas in the capsule isomer **10'** there are 2 Ni doping sites located on both sides of a 5–5 junction. The ground state energies of the isomers **10'** and **11** are higher than that of capsule **10** by 0.65 and 0.59 eV, respectively. For 4 Ni atom doping, capsule **12** is more stable than the isomer **13** by 0.70 eV. These results suggest that the preferred Ni-doping mode is with the dopants far apart.

Second, we consider the B-doped capsules of group **C**. Capsule **18** is the most stable among capsules **16** –**19** that are doped with 2 B atoms. The energies of capsules **16**, **17** and **19** are higher than that of capsule **18** by 0.13, 0.21 and 0.27 eV, respectively. These results suggest that the preferred B-doping mode is with 2 B atoms at para positions in the same 6-membered ring. We use this result for the

B-doping mode selection for capsule **22**. In capsules **20** and **21**, with 4 B atoms, the latter is more stable than the former by 0.11 eV.

The energy gap between the HOMO and the LUMO is an important characteristic of the stability of the ground electronic state. The HOMO–LUMO gap decreases upon capsule elongation from capsule **2** to capsule **3**, similar to cone elongation [63]. In group **B**, metal doping increases the energy gap, especially if the Ni atoms are not clustered together, as for capsules **10** and **12**. In group **C**, B-doping increases the HOMO–LUMO gap only if the doping sites are close together, as in capsules **16** and **21**. The extensive BN doping of capsule **23** increases the energy gap by only 0.03 eV. In group **D**, the Fe atom doping of capsule **24** leads to 0.07 eV increase of the energy gap relative to that of capsule **3**. For capsule **26**, the energy gap is larger by 0.22 eV relative to that of capsule **25**. The wider energy gap and the lower $E_b(ca)$ value of capsule **26** indicate more stable structure relative to capsule **25**. In groups **B** and **C**, the doping modes that lead to the formation of more stable structures, also lead to large energy gaps.

5.3. Spin and charge density in metal-doped nanocapsules

In Table 3, we also list the Mulliken spin density at the metal atom in capsules. Generally, the Ni atom spin densities increase as the ground state multiplicities increase. However, the square-planar complexes tend to have lower Ni atom spin densities. Capsules **7** and **24** are highly spin-polarized, as the spin density of one Ni atom in these structures is zero. The spin polarization effect in capsule **7** is achieved as a result of different Ni(II) coordination. In capsule **24**, the spin polarization arises from doping with different metal atoms. The spin polarization of this structure can be additionally tuned by the attachment of paramagnetic ligands [123,124]. The presence of ground electronic states of high multiplicity together with the energetic closeness of states with different multiplicity suggests that one could easily spin-polarize these systems and make them potentially useful for magnetic applications [125].

In Fig. 9, we show the electron spin density distribution for several capsules. The electron spin density is calculated as the difference between the α (spin-up) and β (spin-down) electron densities. In top left and middle, we show that extension of the B and N doping in capsule **23** leads to spreading of the spin density over larger part of the capsule relative to the undoped capsule **5**. In top right, we show the strong spin polarization induced by the two different metal coordinations at the top and bottom of capsule **7**. The presence of high-spin Fe(II) in capsule **24** also yields a highly spin-polarized structure.

In Table 3, we also list the Mulliken charges on the Ni atom in capsules. In general, the Ni atom charge increases as the ground state multiplicity increases. Consequently, the tetrahedral Ni sites have higher Ni atom charges than the square-planar Ni sites. For capsules **1**–**4**, the Ni atom charge increases as the Ni–N distance increases. It is particularly interesting to see the extensive charge polarization in the asymmetric capsule **7**, caused by the different coordination environment. In group **B**, increased Ni doping causes small charge decrease, as the charge is distributed over several Ni atoms. In group **C**, increased B atom doping causes small increase in the Ni atom charge. The largest metal atom charge is obtained for the Fe atom of capsule **24**. This structure is highly charge polarized, as shown in Fig. 9(bottom right). The smallest metal atom charge is obtained for Ce encapsulated in **25**.

5.4. Optimized geometries of metal-doped nanocapsules

Geometry optimization with DFT of N-doped CNTs has shown that substitutions of C with N atoms lead to less than 0.02 Å shifts in the atomic positions [46,94]. In Table 3, we list selected structural

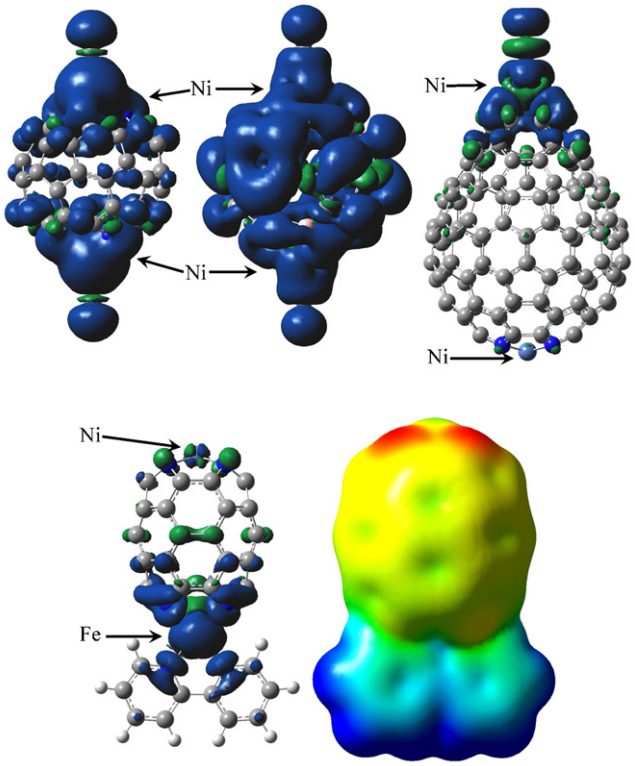

Fig. 9. Electron spin density (ESD) surface (±0.0004 e/bohr^3) of capsules **5** (top left), **23** (top middle), **7** (top right) and and **24** (bottom left). Electrostatic potential (ESP) of capsule **24** in the interval (−0.04, +0.04) *e* mapped on the 0.0004 e/bohr^3 total electron density surface (bottom right).

parameters obtained from the ground-state geometry optimization of the capsules shown in Fig. 7, and the related anionic CLs. Our results are obtained with the B3LYP functional, which is successful in accounting for the relative changes in metal-ligand bond lengths [68]. Due to their extended π-structures, the CLs are rigid and undergo smaller geometrical changes upon metal coordination relative to the respective nanocones [63], mostly observable at the N atom positions. These changes can be quantitatively evaluated from the relative changes in the N-N distance *trans* to the Ni atom.

We also study the metal–N (M–N) bond lengths and N-N-N-M torsion angles in these complexes, and present the results in Table 3. The longest Ni–N bond is obtained for capsule **1** because this structure contains strained 4-membered NiNNC rings. The Ni–N bond length is not affected by elongation of the capsule from **2** to **3**. For capsules **5**, **6** and **7** (top), we note a small Ni–N bond elongation. The Ni–N bond in capsule **7** (bottom) is shorter than that in capsule **4**. This is due to the specific capsule fusion mode that causes contraction of the bottom coordination site. In group **B**, the Ni–N bond lengths show small variations.

In group **C**, B-doping causes large Ni–N bond elongation. This effect is most pronounced in capsules **16**, **17** and **21**, where the B atoms are concentrated near one or several N atoms. This concentration of doping sites in the vicinity of N atoms causes elongation of the nearest Ni–N bond. For capsules **18** –**20** and **22**, we list two Ni–N bond length values. The first value is for N atoms adjacent to the B-doping site and the second value is for the other cases. An interesting effect occurs in capsule **22**, where the 8 B atom doping causes steric strain that is relaxed by elongation of one pair of Ni–N in *trans* position relative to Ni and shortening of the other. For capsule **23**, the B and N doping causes shortening of the Ni–N bonds by 0.05 Å.

In group **D**, the Fe–N(bpy) bond length for capsule **24** is 2.25 Å. This Fe–N bond length is typical for high-spin Fe(II) complexes

[126]. In capsule **25**, the Ce atom is displaced off the CL center, because this atom is too small to be effectively encapsulated. The Ce-N bond lengths are comparable to 2.47 Å, obtained by X-ray adsorption near-edge structure (XANES) determination for the bis(naphthalocyanato) cerium complex [127]. In capsule **26**, the Th atom is almost at the center of the CL, indicating a very effective encapsulation. The Th–N bond lengths in the range 2.71-2.80 Å are reported from X-ray crystallography [128].

The Ni–C bond lengths for capsules **5**, **6**, **7** and **23** are 1.90, 1.94, 1.95 and 1.93 Å, respectively. For capsules **5** –**7**, the Ni–C bonds are shorter than the respective Ni–N bonds, whereas for the B-doped capsule **23** the Ni–C bonds are longer than the Ni–N. In capsule **25**, the Ce–C bond lengths (C atoms bonded to the bottom N atoms, Fig. 7) are 2.53–2.54 Å. It is particularly interesting to consider the Th atom encapsulation in capsule **26**. The Th–C(6-membered ring) bonds of 2.70–2.80 Å are shorter than the Th–N bonds but longer than 2.61 Å reported for Th–C(CO) [129].

5.5. Metal-ligand binding energies in nanocapsules

The metal-ligand binding energies provide a crucial information about the capsule stability. We calculate these energies for hemolytic (E_b) dissociation, i.e. dissociation yielding neutral metal atoms and ligands.

$$E_b(ca) = [E(\mathrm{n}) - E(\mathrm{CL}) - E(\mathrm{M}) - E(\mathrm{CN})]/m. \quad (5)$$

Here, E(n) is the total energy of capsule n, E(CL) is the total energy of the neutral singlet CL, E(M) is the total energy of all *isolated* metal atoms in the singlet state, E(CN) is the energy of the doublet CN^0, and m is the number of metal atoms in the capsule. The E_b energies are obtained per metal coordination site, except for the asymmetric capsules **7** and **24**, where we calculate E_b for each metal atom separately. The binding energy of the Ni atom at the top of capsule **7** is $E_b(\mathrm{Ni}(\mathbf{7}_{top})) = E(\mathrm{n}) - E(\mathrm{CL{+}Ni}_{bottom}) - E(\mathrm{Ni}) - E(\mathrm{CN})$, where $E(\mathrm{CL{+}Ni}_{bottom})$ is the total energy of the structure that contains the CL of **7** and the bottom Ni atom, optimized in doublet state. Similarly, binding energy of the N atom at the bottom of capsule **7** is $E_b(\mathrm{Ni}(\mathbf{7}_{bottom})) = E(\mathrm{n}) - E(\mathrm{CL}) - 2E(\mathrm{Ni}) - E_b(\mathrm{Ni}(\mathbf{7}_{top})) - E(\mathrm{CN})$. The binding energy of the Fe atom at the bottom of capsule **24** is $E_b(\mathrm{Fe}) = E(\mathrm{n}) - E(\mathrm{CL}) - E(\mathrm{Ni}) - E(\mathrm{Fe}) - E_b(\mathrm{Ni}(\mathbf{3})) - E(\mathrm{bpy})$, where E(bpy) is the total energy of a neutral singlet bpy ligand and E(Fe) is the total energy of a singlet Fe atom. The capsule and ligand energies are obtained for the optimized geometries of the structures. Thus, the energy changes arising from the changes in geometry that occur as a result of the bonding are included in the $E_b(ca)$.

The $E_b(ca)$ values are listed in Table 3. Low negative $E_b(ca)$ values indicate strong metal-ligand bonds. In group **A**, the binding energy of capsule **1** is the highest, because of its strained geometry. The $E_b(ca)$ value of capsule **3** is lower than that of capsule **2**, suggesting that capsule elongation relieves strain. The $E_b(ca)$ value of capsule **4** is rather high, considering that the torsion angle does not suggest large strain. It could arise from a large geometry rearrangement upon Ni coordination and/or short N-N distances that do not allow for effective Ni coordination. The binding energies of capsules **5** and **6** that contain hexadentate CLs are higher than these of capsules **1** –**4**. The stronger binding in capsule **5** relative to **6** is supported by the shorter Ni–N bond and the smaller torsion angle that is closer to the perfect tetrahedron value of 35.3°. In the asymmetric capsule **7**, $E_b(ca)$ for the top Ni atom is 2 eV higher than for the bottom one. In this structure, the top and bottom Ni atom binding energies are also higher than these of capsules **6** and **4**, respectively, that have analogous coordination sites. The stronger binding in the asymmetric structure **7** could be due to strain relief at the fusion area.

In group **B**, the binding is weaker for structures that contain Ni atoms close together, as in **9**, **11** and **13**, relative to **4**, **10** and **12**. This trend is supported by the capsule stability as evaluated from the total energies. Additional Ni doping also increases the binding strength.

In group **C**, the binding is stronger than for the undoped capsule **2**. Increased B-doping for capsules **21** and **22** leads to increased Ni binding strength relative to capsules **16** –**20**. Also, B-doping near one Ni atom for capsules **16** and **21** increases the binding strength relative to capsules **17** and **20**, respectively. For capsule **23**, both B and N doping decrease the binding energy by 0.80 eV relative to the undoped capsule **5**.

In group **D**, the high Fe atom binding strength for capsule **24** is due to its octahedral coordination. The Th binding energy for capsule **26** is higher than for capsule **25**. Our results for U, Th and Ce encapsulation in the CL of capsule **2** show that this CL is particularly effective for Th binding and could be used for selective Th(IV) sequestration. For capsules **2** –**6**, the $E_b(ca)$ values show that the Ni–Cl bond is weaker than the Ni-cone bonds reported previously [63]. This is because the capsules are more rigid than the respective cones.

6. Applications of metal-doped carbon nanostructures

We have shown that various metallic binding sites could be introduced into carbon nanostructures, with minimal structural changes. In principle, the coordination sites might be finely tuned by the nature of the transition metals and the location of the doping sites. These metal-doped and functionalized nanosystems can possess interesting chemical, electronic, optical and mechanical activities that we briefly discuss here.

6.1. Catalysis with Fe-xN-doped nanostructures

The development of proton exchange membrane fuel cells [38] holds exceptional promise for the use of hydrogen in efficient power generation for mobile applications [130,38]. The energy conversion efficiency is predominantly limited by the activity of electrocatalytic oxygen reduction reaction (ORR) [131] on the cathode side. Presently, the best catalysts for ORR are based on costly precious metals (Pt, Pd) [132,133] and their bimetallic combinations with Ni and Co [134,135]. There is a need for the non-precious and low-cost catalysts [136], and iron-based catalysis is one of the promising directions [137].

The metal–nitrogen centers in carboneous nanosystems described above might serve as *highly stable* catalysts on a large surface area support [65]. The geometry of nanotube arrays provides confined space which can be used for shape-selective chemistry in heterogenous catalysis and electrocatalysis. CNTs could provide very high stability and density of the catalytic sites if the catalyst can be effectively *anchored* to the nanotube walls and *dispersed* over the whole tube. CNTs also have the largest thermal conductivity, which might significantly slow down the degradation processes during catalysis. In this study, we combine theoretical and experimental approaches to design and investigate the stability of porphyrin-like Fe-xN catalytic sites embedded in CNTs.

Recently, simultaneous doping of CNTs by Fe and N was experimentally realized [138]. The structure of the active sites was characterized using X-ray absorption near edge spectroscopy (XANES) and EXAFS at the energy of Fe K-edge Here, we show for comparison the χ-functions extracted from the EXAFS data with the calculated data from our optimized structures [65].

In Fig. 10, we compare the experimental and calculated EXAFS spectrum of Fe(II) phthalocyanine used as a reference compound, where the theoretical spectrum is based on our optimized structure. We shift the calculated spectrum by 0.46 $Å^{-1}$ to equally match the first and the second minima in the experimental spectrum. In our calculations, we use a scattering path of 5.5 Å, which includes atoms

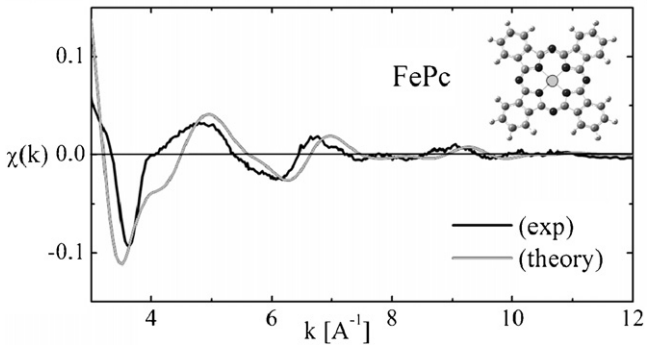

Fig. 10. Experimental (exp) and calculated (theory) EXAFS spectra of iron-phthalocyanine (FePc).

up to the second nearest neighbor of iron. We also include thermal motion and attenuate the amplitude of $\chi(k)$ by using the Debye-Waller factors determined for phthalocyanine[139], $\sigma^2 = 0.005$ Å^2. FEFF calculations with the same parameters and same shift are performed.

In Fig. 11 (a, b), we show the absorption coefficient functions $\chi(k)$ extracted from the EXAFS spectra of the experimentally prepared catalytic Fe-xN sites in aligned CNTs. These experimental results are compared with our simulations using the FEFF package for the optimized Fe–2N and Fe–4N structures. The Fe-xN structures with the lowest substitution energy, namely (8,0) Fe–4N (AX(py)) and (7,0) Fe–2N (1–3) structures shown in Fig. 3 and Fig. 1, provide a close match with the peaks of the experimental χ-functions. The similarity of the spectra indicates that the experimentally prepared structures can be formed by a superposition of the Fe–2N and Fe–4N structures.

In Fig. 11(c), we show the linear combination of Fe–2N and Fe–4N spectra, given by $\chi(k)_{\text{theory}} = \alpha\chi(k)_{\text{Fe-2N}} + \beta\chi(k)_{\text{Fe-4N}}$, that

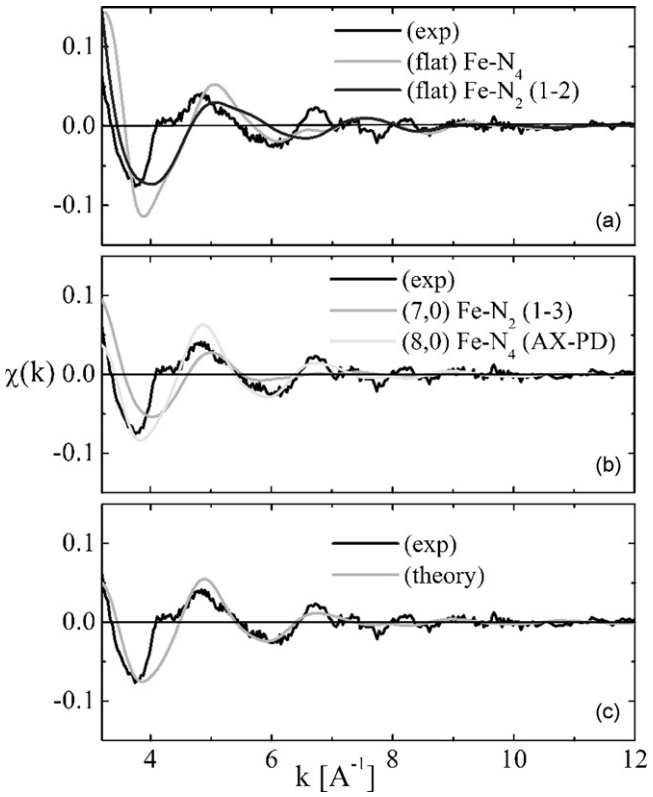

Fig. 11. Experimental and calculated absorption coefficient functions $\chi(k)$ for (a) flat graphene clusters and (b) bent clusters. (c) Linear combination of the Fe–2N and Fe–4N spectra for structures with the lowest substitution energy optimized to fit to the $\chi_{\text{exp}}(k)$. The resulting curve contains 22.26% and 77.74% contributions from the Fe–2N and Fe–4N configurations, respectively.

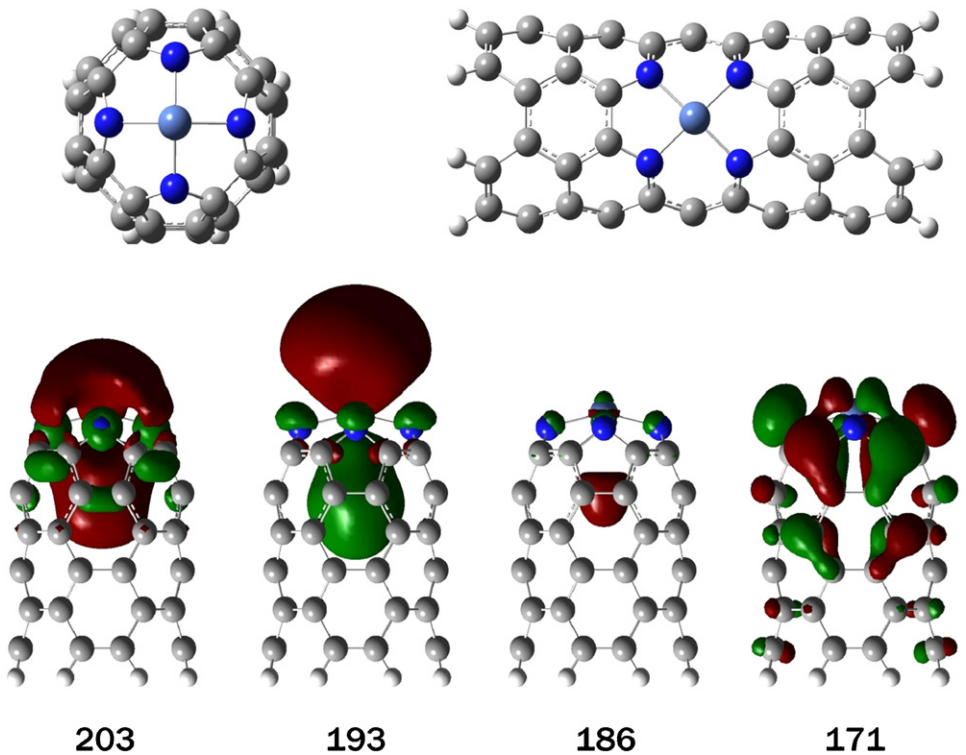

Fig. 12. (up left) Top view of the Ni-doped cone and (up right) (4,4) CNT. (down) Extended MOs of the Ni-doped cone with a large metallic content. (left to right) The MOs with large composition of the 5s Ni-orbital ($E_{203} = 2.64$ eV), the 11 px Ni-orbital ($E_{193} = 1.06$ eV) and the 6s Ni-orbital ($E_{186} = 0.24$ eV). (last) The HOMO is more spread on the cone and less away from it ($E_{171} = -5.55$ eV).

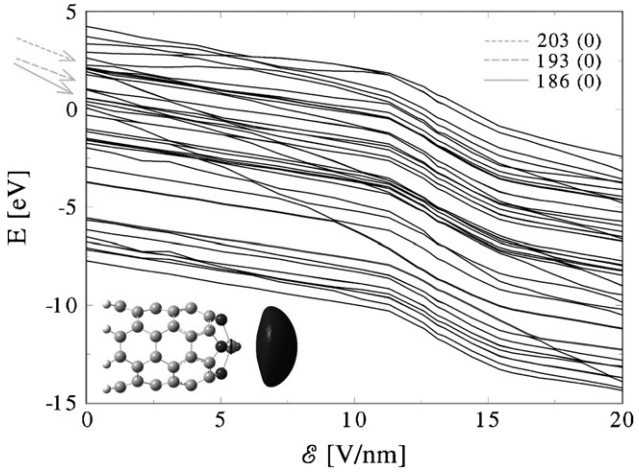

Fig. 13. Dependence of the neutral Ni-doped nanocone MO energies on the strength of the electric field $\mathcal{E}$. The HOMO and the LUMO are shown by thick lines. The extended Ni-orbitals drop fast with $\mathcal{E}$. (inset) The HOMO at electric field of 15.4 V/nm that contains mostly Ni *s* orbital contribution.

shows the best agreement with $\chi_{exp}(k)$. In the optimization, we use a least-square-fitting method that gives the composition ratio of $\alpha/\beta = 0.29$ between the chosen Fe–2N and Fe–4N configurations. The combined spectrum shows that the two types of sites might be observed in the experiments [65].

Catalytic activity of transition metal macrocyclic complexes towards oxygen reduction is often correlated with a first ionization potential of the complexes, since the electron is extracted from the d-states of the metal atom. Vertical ionization potentials of metal-doped CNTs are found to be in the range of 4.5 to 5.75 eV, depending on CNT curvature [65], which is well below the reported values for Fe-porphyrins of 6.36 eV [140]. The ionization potentials of pristine CNTs are about 4.86-5.08 eV [65](experiment 4.6–4.8 eV [141]). The lower IP of metal-doped CNTs relative to Fe-porphyrins is due to the hybridization of iron d-states and carbon p-states, as indicated by out molecular orbital results. The lower ionization potential is often related to a lower redox potential and a higher oxidation activity [92]. Therefore, we expect Fe–4N complexes in CNTs to be more active in ORR as compared to other iron macrocycles. Our preliminary calculations of dioxygen adsorption on iron atom in Fe–4N structures give O_2 binding energies of 0.78 eV for (7,0) CNT cluster, which is similar to that of porphyrins [92].

6.2. Electric field control of atom adsorption on doping metallic sites

Spatially extended Rydberg states that form in atoms and molecules can have numerous applications [142,143]. We have suggested that extended states could also form above metallic CNT [144,145], when electrons spin around their mirror images in the CNTs. Recently, these "tubular image states" with long lifetimes were observed in photo-excitation experiments [146]. Here, we

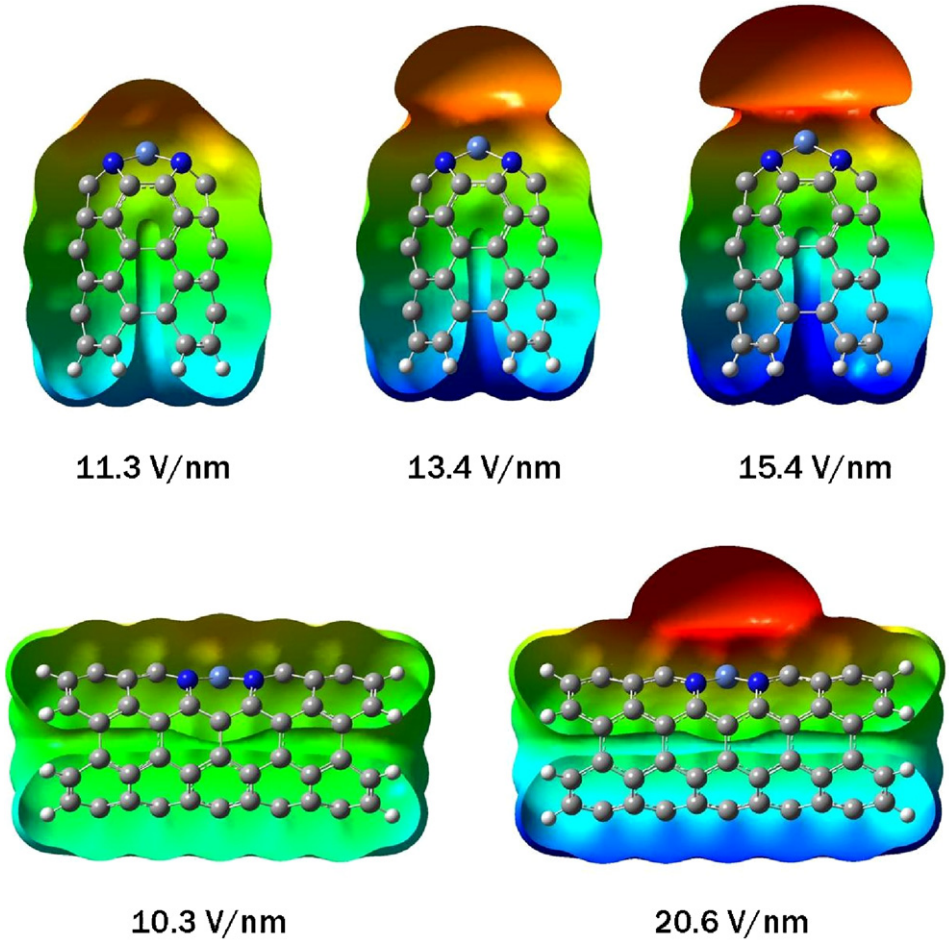

Fig. 14. (Up left to right) Extraction of the electron density from the Ni-doped nanocone in the static electric field $\mathcal{E} = 11.3$, 13.4 and 15.4 V/nm. (down) Extraction of the electron density from the Ni-doped (4,4) CNT in $\mathcal{E} = 10.3$ (left) and 20.6 V/nm (right). In all the structures, the electrostatic potential in the interval $\varphi = (-5.4, +5.4)$ V is mapped on the surface of the constant electron density 0.0004 e/Bohr^3.

show that extended electronic states formed above metal-doped carbon nanostructures can be controlled by using external electric field [66]. We also show how one can use electric fields to control ion adsorption to and desorption form the metallic sites.

In Fig. 12 (up), we present the Ni-doped tip of cone **3** (Fig. 4) and wall of a (4,4) single-wall CNT. In the left structure, Ni is attached to the four pyrrole rings [63], as in metallo-porphyrins [53], but the four connecting methine linkers are removed. In the right structure, two C atoms are replaced with the Ni atom and the four adjacent C atoms are substituted with four N atoms [47]. Cone **3** is selected because it has only one axial ligand coordination site [63]. Both complexes are ended with H atoms that eliminate their dangling bonds. Their electronic structures and geometries are calculated and optimized (in static electric fields) in the singlet states by using B3LYP/6-311G*[69,68,75,76].

In Fig. 12(down), we show several extended molecular orbitals (MO) with a significant 4-6*s* Ni-atomic orbital composition and a large probability density formed above the surface of the neutral nanocone, in the absence of electric field. These MOs are less spread on the cone than the HOMO, shown last, and are shifted ≈ 6 eV above it, in the unbound part of the spectrum. In order to facilitate their population by one-photon processes, we can shift them closer to the HOMO by electric fields $\mathcal{E}$ in the Stark effect [147].

In the linear Stark effect [147], the energy of a state $\langle .|\Psi\rangle$ with no parity shifts in the static electric field $\mathcal{E}$ by $\Delta E = -\mathcal{E}\langle\Psi|d|\Psi\rangle$, where $d = er$ is the dipole operator. Other states might be shifted by the quadratic Stark effect [147]. Note that although carbon-capped single-walled CNTs are, in principle, stable at fields $\mathcal{E} < 20$ V/nm [148,149], their states are in fact metastable and can significantly emit electrons by tunneling at fields $\mathcal{E} > 3 - 5$vV/nm [150].

In Fig. 13, we present the electronic spectrum around the HOMO in the Ni-doped nanocone from Fig. 12, calculated in electric fields, $0 < \mathcal{E} < 20$ V/nm, oriented up along its axis. While the absolute shift of all the MOs depends on the position of the center of mass of the structure used in *ab initio* calculations (e φ- term), the relative positions of the MOs are invariant on the center position. We can see that some virtual orbitals move faster and form avoided crossing regions with other MOs on their way. The slowly shifting MOs are mostly composed of atomic orbitals of the aromatic carbon atoms. If electric field is applied parallel to the plane of benzene, the fastest energies fall at a rate of $E \approx 0.4$ eV per V/nm [151], which is close to $E \approx 0.3$ eV per V/nm valid for these MOs in Fig. 13.

The fast moving MOs in Fig. 13 are mostly composed of the extended 4-6*s* Ni-orbitals with large dipole matrix elements. They shift by the nonlinear Stark effect that dominates at higher fields. The zero-field 186-th MO, depicted in Fig. 12, moves the fastest, at a rate of $E \approx 0.7$ eV per V/nm, which is close to that of the 4*s* Li-orbital in such fields, equal to $E \approx 1.1$ eV per V/nm [152]. These MOs eventually reach the HOMO and become populated. At fields $\mathcal{E} \approx 10 - 11$V/nm, an avoided crossing between the new LUMO (186-th MO moving down) and the HOMO is formed, which leads to shrinking of the HOMO–LUMO gap. At fields $\mathcal{E} > 15$ V/nm, this MO moves below the HOMO. Large electric-field-induced effects were also observed in BN nanotubes [153] and linear semiconductor nanocrystals [154].

The fast shifting extended MOs become eventually populated. In Fig. 14 (up left to right), we show the total electron density in the neutral Ni-doped nanocone for the electric field $\mathcal{E} = 11.3$, 13.4 and 15.4 V/nm, respectively. One can see the extraction of charge and formation of an extended "electron bag" above the cone, formed by the populated extended MOs. In Fig. 14(down), we show the same in the metal-doped wall of the (4,4) single-walled CNT from Fig. 12, for the fields $\mathcal{E} = 10.3$ and 20.6 V/nm, oriented orthogonal to the plane with the four Ni atoms.

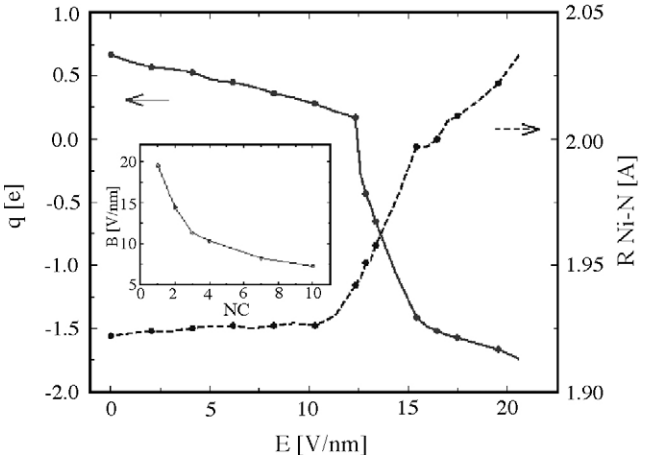

Fig. 15. Dependence of the Ni atom Mulliken charge and the average Ni–N distance on the strength of the electric field for the Ni-doped nanocone. (inset) Dependence of the electric field needed for the filling of the extended states on the length of the nanocone (number of CNT's elementary cells).

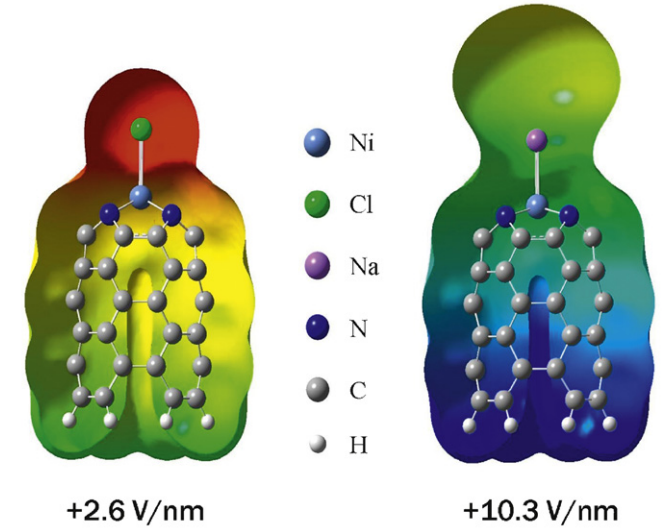

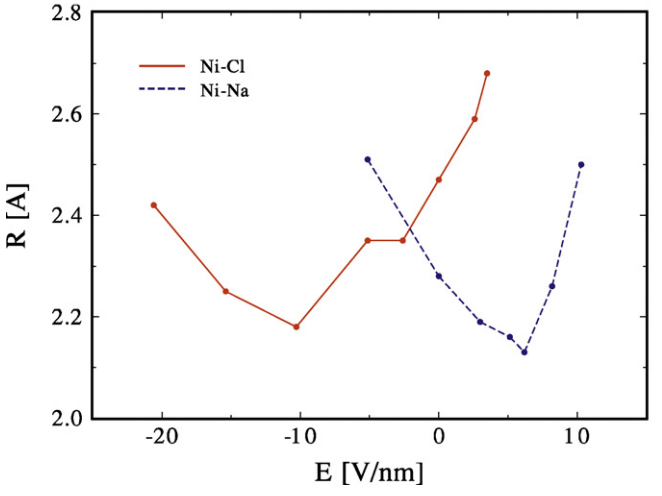

Fig. 16. Binding of the Cl^- and Na^+ ions to the cone. (left) Extraction of Cl^- at $\mathcal{E} \approx +2.6$ V/nm and Na^+ in $\mathcal{E} = +10.3$ V/nm. (right) The Ni–Cl and Ni–Na distances as a function of the field strength.

Coulombic coupling between the extended (populated) and other MOs leads to restructuralization of the system. As we illustrate in Fig. 15, in the field $0 < \mathcal{E} < 11$ V/nm, the positive Ni-atom charge gradually decreases, whereas the average Ni–N bond length increases. In the fields $\mathcal{E} \approx 12 - 15$ V/nm, these changes become much larger, since the HOMO gains a Ni character. At $\mathcal{E} \approx 12.5$ and 15 V/nm, we can see breaks both in Figs. 13 and 15. At $\mathcal{E} \approx 15$ V/nm, the Ni-states continue to move down and the HOMO is formed by other states. Finally, above $E = 20$ V/nm, the Ni–N bonds cleave.

In the inset of Fig. 15, we show the dependence of the "minimum field" necessary for the electron extraction on the number of CNT elementary cells, N_C, in the nanocone ($N_C = 2$ in the structure from Fig. 14(up)). The field is substantially decreased for longer cones, since their polarization is larger, which means that they could provide more electrons to the tip of the cones. In this way, one could populate the extended MOs even before the field gets too large, and the field-induced electron emission becomes significant, especially, if this process is combined with their photo-excitation.

The electric field needed for filling of the extended MOs also depends strongly on the charge of the cone. For the cone in Fig. 14 with the charge of $+2e$, $+1e$, $-1e$ and $-2e$ the extraction field is 18.2, 13.8, 7.5 and 6.5 V/nm, respectively (structures with odd number of electrons are calculated in triplet states). Its decrease with the increase of the number of electrons is due to the shift of the HOMO up, leading to the formation of the avoided crossing with the extended states at lower fields. Also, the electron extraction from positively charged cones requires higher field because the MOs of cations are bound stronger. These results agree with the decrease of the extraction field for longer cones, shown in the inset of Fig. 15, where more electrons are effectively available at the cone tips at weaker fields, as the cone length is increased.

In the fields of several V/nm, these extended MOs could have field-emission lifetimes of tens of fs, in analogy to other 4-6*s* atomic orbitals [152]. On the other hand, CNTs in the field of $\mathcal{E} = 3$ V/nm have field-emission currents of $j \approx 1$ nA [150], i.e. one electron leaves every $\approx$ 160ps. This slow electron emission very likely goes from a localized state [155] or adsorbate on the CNT [156,157] that are slowly repopulated after each event. Since filling of the extended states in metal-doped nanocones might be more easily controllable, they could be used in tunable electron emitters [148,149,156].

The metal-doped nanocones might also be used to manipulate chemical bonds, ions, atoms or molecules, in analogy to scanning tunneling microscopy (STM) [158], atomic force microscopy (AFM) [159] and other techniques [160]. In Fig. 16, we present the binding of Cl^- and Na^+(from NaCl) to the cone tip at varied field strength. In Fig. 16(right), we show that Cl^- anion binds to the positively charged Ni in the range of fields: $-15.4 < \mathcal{E} < +2.6$ V/nm, where the Ni—Cl bond length is varied (the charged structure is calculated in the singlet state). Chloride detaches from the cone tip at $\mathcal{E} + 2.6$ V/nm. In the field range $+5.1 < \mathcal{E} < +10.3$ V/nm, Na^+ forms a weak bond with Ni. In Fig. 16(left), we show that by increasing the field to $\mathcal{E} = +10$ V/nm in the Na^+-nanocone system causes extensive extraction of the electron density. These electrons bind the Na^+ and Ni, but at fields $\mathcal{E} < +5$ V/nm they "return" to the structure, causing the release of Na^+. Thus, electric fields can control bonding and releasing of ions to the metal-doped nanocone.

6.3. Light-harvesting antennas

In Fig. 17, we also present a light-harvesting antenna based on the metal-doped nanocones and nanocapsules [64]. We can see the HOMO-2 (next nearest to the HOMO), HOMO and LUMO diagrams of this system ($H_{26}C_{66}N_{18}S_2RuReOs$). In order to spatio-energetically separate its active quantum states, we order the metals so that the polyimine moiteies have decreasing metal-to-ligand charge transfer state energies, from Re(I) and Ru(II) to Os(II) [161,162]. Therefore, the system is formed by a cone [63] containing an Os(II) atom on the tip that is coordinated to a 2,2'-bipyrimidine ligand (bpm) [163]. The latter is coordinated at the top to the Ru(II)-doped tip of a capsule derived from **21**, while the other tip of the capsule is doped with a Re(I) atom coordinated to a 4,4'-dithiopheno-2,2'-bipyridine (dtbpy) ligand. The capsule of this closed-shell neutral antenna contains four B atoms as in capsule **21** and one B atom in para position. The B-doping mode of capsule **21** is selected because it yields the largest HOMO–LUMO gap in series **C** (Table 3). The B atom doping at the para position yields the most stable structure among capsules **16**–**19**.

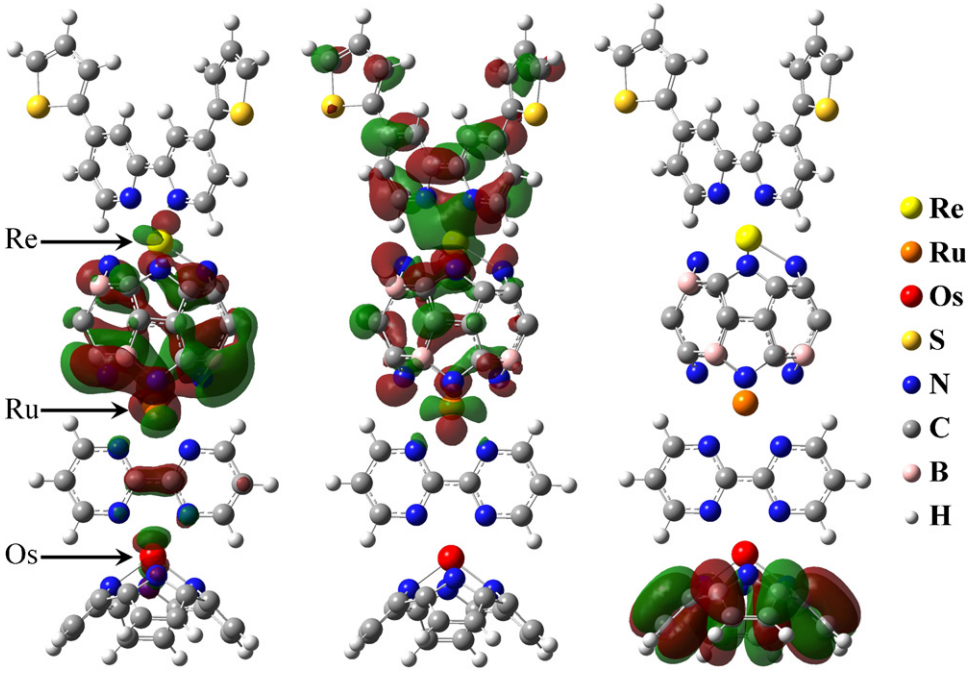

Fig. 17. (left) Frontier molecular orbitals HOMO-2, (middle) HOMO and (right) LUMO of a sandwich-like light-harvesting antenna.

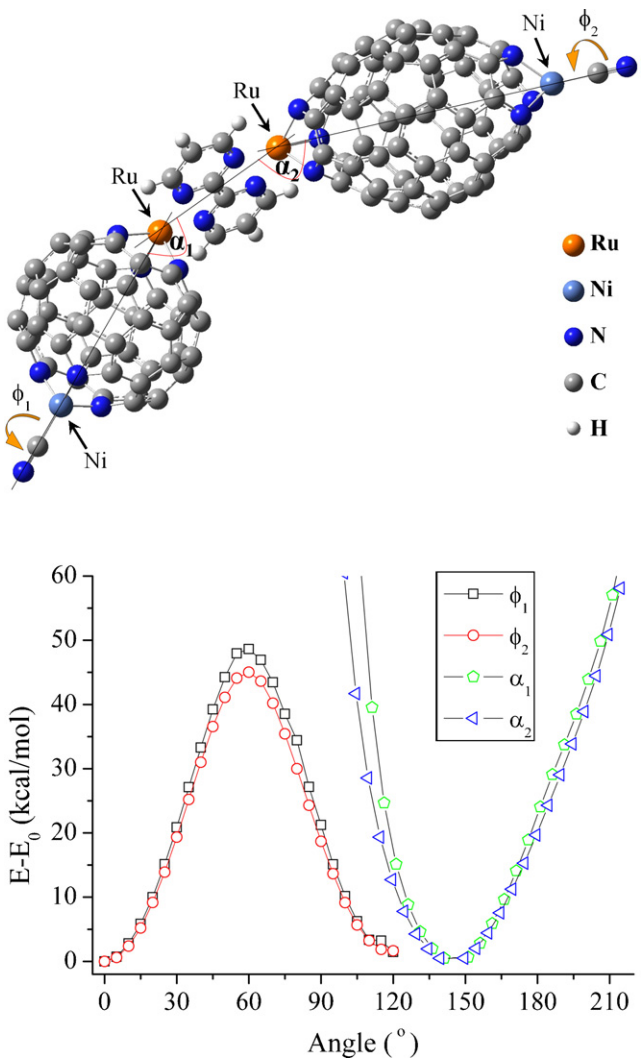

Fig. 18. (Top) A nanomechanical system formed by two extended capsules coordinated to a bpm ligand. The system can be displaced from its equilibrium bent conformation by bending and twisting. (bottom) The relative energy of the nanomechanical system for twisting and bending. The E and E_0 are the total energies of the bent (twisted) and optimized structures, respectively.

This sandwiched system allows large *spatial* separation of its frontier orbitals, necessary in photovoltaic conversion [164]. Its HOMO–LUMO energy gap is 1.38 eV, and the energy of the HOMO-2 is 0.21 eV lower than the HOMO. The B-doping and thiophene covalent bonding increase the HOMO–LUMO gap by ≈0.8 eV, shifting it near the visible light range relative to the structure that contains capsule **2** and bpy. Chen et al. have shown that the electron-rich thiophene moiety covalently bonded to bpy increases the HOMO–LUMO gap of Ru(II) photosensitizers [165]. The light-induced electronic transitions can occur from the HOMO and HOMO-2 that contain large Re-dtbpy and Ru-capsule orbital contributions, respectively, to the LUMO. The latter is strongly localized on the carbon part of the nanocone [63] and should allow efficient charge collection at the electrode. The system is also highly rigid, preventing thus parasitic effects, such as electron tunneling.

6.4. Nanomechanical systems

Finally, we present in Fig. 18 (top) a *nanomechanical system* ($H_6C_{118}N_{18}Ni_2Ru_2$), formed by two bimetallic capsules **5** and **6**, having two Ru and two Ni atoms, coordinated via a bridging tetradentate bpm ligand. We use the fourth period d^6 Ru atoms instead of d^8 Ni atoms, because the former can better accommodate the five-coordinate ligand environment. The ground state of this structure is a heptet and its energy gap is 0.68 eV. The equilibrium bending of the structure is caused by different symmetries of the capsules (threefold) and the ligand (twofold) around the two Ru atoms as well as by the different capsule coordination sites. In a series of single-point calculations, we calculate the energies of bending about angles α_1 and α_2, as well as twisting (spinning) about angles ϕ_1 and ϕ_2. The spinning axes for ϕ_1 and ϕ_2 are defined as the median lines for the lower left and upper right capsules (inclusive of Ru, Ni and CN), respectively. The bending for α_1 and α_2 is done in the plane defined by the Ni atoms at the bottom left and top right, respectively, as well as the 2 Ru atoms. In the optimized structure, the values of α_1 and α_2 are 146.2 and 144.5 °, respectively. The angles are varied one at a time, while the rest of the structure remains unchanged.

In Fig. 18(bottom), we show the dependence of the system total energy on the twisting and bending angles, where the zero values of ϕ_1 and ϕ_2 correspond to the optimized structure. The ϕ_1-angle twisting barrier is higher than the ϕ_2-barrier by 5.0 kcal/mol. The bending energy dependence shows that the system is more rigid with respect to angle α_1 than α_2. The system is more rigid towards decreasing of α_1 and α_2 than towards increasing them relative to the optimized values. The complex resembles a joint in arms or legs and might be used in nanomechanics.

7. Conclusions

We have reviewed *ab initio* results obtained for metal, nitrogen and boron doped graphene, CNTs, carbon nanocones and nanocapsules. The results can be summarized as follows:

1. Iron binding in both Fe–2N and Fe–4N embedded in graphene and CNT is stronger than in the pristine structures. The strongest Fe binding is predicted to occur in pyridine-like Fe–4N configurations. The agreement between experimental and simulated EXAFS spectra allows us to conclude that Fe–4N are the most probable active sites present in experimental systems [65]. Such active sites might provide unique catalytic activity, particularly where substrate hydrophobicity and electrical conductivity are critical. The geometry of these nanoporous catalysts provides confined spaces decorated with transition metal atoms, which offers new opportunities for shape selectivity.
2. Metallo-pyrrole and metallo-pyridine moieties embedded in the tips of carbon nanocones allow for controlled binding of important ligands. The increase in the nanocone size causes a decrease in the metal atom charge and enhances its ability to bind ligands through π-backbonding and σ-donation. The carboneous skeleton of the presented structures provides possibilities for electronic control of the axial ligands [63].
3. In metal-doped nanocapsules, the preferred metal doping patterns contain metal atoms that are not in close proximity, whereas the preferred B-doping sites have B atoms separated by 2 C atoms. Additional B and N doping increases the ground state spin multiplicity, binding energy and HOMO–LUMO gap, thus increasing capsule stability. The CLs can selectively encapsulate heavy metal ions. For the CL that is structurally related to C_{36}, Th(IV) forms the most effective bonding, suggesting that these structures could be used as size-selective sequestration agents [64].
4. These nanostructures could be used in catalysis [65] and various multifunctional devices, such as nanomagmets, light-harvesting antenna or nanomechanical systems [64]. The extended electronic states formed above metal-doped carbon nanostructures and controlled by using electric field can be employed for bind-

ing of ions and molecular ligands, and be used in catalysis and nanodevices [66].

Although, we have designed and modeled the metal-doped nanostructures by standard first principle methods, precise description of these systems might be done more efficiently by specialized techniques. In general, the ligand binding preferences of complex multifunctional systems can be predicted by using reactivity descriptors based on the hard and soft acid and base (HSAB) theory. This has been demonstrated for extended carboneous systems [166–173] and other surfaces [174,175].

The described metal-doped carbon nanostructures might be experimentally realized with advanced chemical methods [176], allowing substitutions of selected carbon atoms or via a direct stepwise synthesis. In the first step of such a synthetic approach, one could prepare the structure framework with a nitrogenated rim(s). The opening can be realized by electron beam cutting or by etching in solution [177]. The subsequent nitrogenation can be done by using transient arc discharge [47]. In the second step, we could coordinate the transition metal atom to the nitrogenated rim. More refined structures might be possible to prepare in a series of ring closure "molecular surgery" reactions [178–180]. The metal binding to various ligands can be optimized by introducing further B and N substitutions [181]. The chemical vapor deposition method of Yang et al. for preparation of Fe–4N catalytic site built-in CNT walls could be extended to fullerenes [138]. The solvent-free approach for synthesis of pyrogallol[4]arene nanocapsules is also attractive [182].

The introduction of transition metal atom binding sites into non-metallic nanostructures has a potential for producing active nanosystems. These metal sites allow binding of ligands that bring the additional functionality. The doped cones, capsules and tubes might be applied in chemistry, as novel catalysts or drug carriers, and could form a large mosaic of universal building blocks ready for use in molecular electronics and nanoscale machinery. These systems form a bridge between traditional nanostructures and molecules encountered in organic chemistry and biochemistry, and should be of great interest for their potential role in future nanodevices.

Acknowledgments

This work was partially supported by the National Computational Science Alliance (NCSA) and the National Energy Research Scientific Computing Center (NERSC).

References

[1] H.W. Kroto, J.R. Heath, S.C. Obrien, R.F. Curl, R.E. Smalley, Nature 318 (1985) 162.
[2] C. Piskoti, J. Yarger, A. Zettl, Nature 393 (1998) 771.
[3] H. Prinzbach, A. Weller, P. Landenberger, F. Wahl, J. Worth, L.T. Scott, M. Gelmont, D. Olevano, B. von Issendorff, Nature 407 (2000) 60.
[4] S. Iijima, Nature 354 (1991) 56.
[5] S. Iijima, T. Ichihashi, Y. Ando, Nature 356 (1992) 776.
[6] Y.P. Sun, K.F. Fu, Y. Lin, W.J. Huang, Acc. Chem. Res. 35 (2002) 1096.
[7] A. Krishnan, E. Dujardin, M.M.J. Treacy, J. Hugdahl, S. Lynum, T.W. Ebbesen, Nature 388 (1997) 451.
[8] G.Y. Zhang, X. Jiang, E.G. Wang, Science 300 (2003) 472.
[9] K.S. Novoselov, A.K. Geim, S.V. Morozov, D. Jiang, M.I. Katsnelson, I.V. Grigorieva, S.V. Dubonos, A.A. Firsov, Nature 438 (2005) 197.
[10] D.A. Dikin, S. Stankovich, E.J. Zimney, R.D. Piner, G.H.B. Dommett, G. Evmenenko, S.T. Nguyen, R.S. Ruoff, Nature 448 (2007) 457.
[11] F. Schedin, A.K. Geim, S.V. Morozov, E.W. Hill, P. Blake, M.I. Katsnelson, K.S. Novoselov, Nat. Mater. 6 (2007) 652.
[12] M. Dresselhaus, G. Dresselhaus, P. Eklund, Science of Fullerenes and Carbon Nanotubes, Academic Press, San Diego, 1996.
[13] R.S. Lee, H.J. Kim, J.E. Fischer, A. Thess, R.E. Smalley, Nature 388 (1997) 255.
[14] M. Terrones, A.G. Souza, A.M. Rao, Carbon Nanotubes 111 (2008) 531.
[15] P. Avouris, Z.H. Chen, V. Perebeinos, Nat. Nanotechnol. 2 (2007) 605.
[16] M. Terauchi, M. Tanaka, K. Suzuki, A. Ogino, K. Kimura, Chem. Phys. Lett. 324 (2000) 359.
[17] A.H. Nevidomskyy, G. Csanyi, M.C. Payne, Phys. Rev. Lett. 91 (2003) 105502.
[18] B. Wang, P. Král, Small 3 (2007) 580.
[19] K. Sint, B. Wang, P. Král, J. Am. Chem. Soc. 130 (2008) 16448.
[20] X. Lepro, E. Terres, Y. Vega-Cantu, F.J. Rodriguez-Macias, H. Muramatsu, Y.A. Kim, T. Hayahsi, M. Endo, T.R. Miguel, M. Terrones, Chem. Phys. Lett. 463 (2008) 124.
[21] Y.Y. Shao, J.H. Sui, G.P. Yin, Y.Z. Gao, Appl. Catal. B 79 (2008) 89.
[22] V. Meunier, P.S. Krstic, J. Chem. Phys. 128 (2008) 041103.
[23] N.G. Chopra, R.J. Luyken, K. Cherrey, V.H. Crespi, M.L. Cohen, S.G. Louie, A. Zettl, Science 269 (1995) 966.
[24] D. Golberg, Y. Bando, C.C. Tang, C.Y. Zhi, Adv. Mater. 19 (2007) 2413.
[25] T. Oku, T. Kusunose, T. Hirata, R. Hatakeyama, N. Sato, K. Niihara, K. Suganuma, Diamond Related Mater. 9 (2000) 911.
[26] P. Král, E.J. Mele, D. Tomanek, Phys. Rev. Lett. 85 (2000) 1512.
[27] E.J. Mele, P. Král, D. Tomanek, Phys. Rev. B 61 (2000) 7669.
[28] A. Hirsch, Ang. Chem. Int. Ed. 41 (2002) 1853.
[29] D. Tasis, N. Tagmatarchis, A. Bianco, M. Prato, Chem. Rev. 106 (2006) 1105.
[30] J. Ozaki, N. Kimura, T. Anahara, A. Oya, Carbon 45 (2007) 1847.
[31] M. Zheng, A. Jagota, M.S. Strano, A.P. Santos, P. Barone, S.G. Chou, B.A. Diner, M.S. Dresselhaus, R.S. McLean, G.B. Onoa, G.G. Samsonidze, E.D. Semke, M. Usrey, D.J. Walls, Science 302 (2003) 1545.
[32] S. Banerjee, T. Hemraj-Benny, S.S. Wong, Adv. Mater. 17 (2005) 17.
[33] Y.M. Zhang, D.J. Zhang, C.B. Liu, J. Phys. Chem. B 110 (2006) 4671.
[34] S.S. Wong, E. Joselevich, A.T. Woolley, C.L. Cheung, C.M. Lieber, Nature 394 (1998) 52.
[35] N.W.S. Kam, T.C. Jessop, P.A. Wender, H.J. Dai, J. Am. Chem. Soc. 126 (2004) 6850.
[36] R. Jasinski, Nature 201 (1964) 1212.
[37] E. Yeager, Electrochim. Acta 29 (1984) 1527.
[38] B.C.H. Steele, A. Heinzel, Nature 414 (2001) 345.
[39] E.B. Easton, A. Bonakdarpour, J.R. Dahn, Electr. Solid State Lett. 9 (2006) 463.
[40] M. Lefevre, J.P. Dodelet, Electrochim. Acta 48 (2003) 2749.
[41] J. Maruyama, I. Abe, J. Electrochem. Soc. 154 (2007) 297.
[42] J.H. Zagal, Coord. Chem. Rev. 119 (1992) 89.
[43] F. Jaouen, F. Charreteur, J.P. Dodelet, J. Electrochem. Soc. 153 (2006) 689.
[44] C. Medard, M. Lefevre, J. Dodelet, F. Jaouen, G. Lindbergh, Electrochim. Acta 51 (2006) 3202.
[45] K. Gong, F. Du, Z. Xia, M. Durstock, L. Dai, Science 323 (2009) 760.
[46] C.P. Ewels, M. Glerup, J. Nanosci. Nanotechnol. 5 (2005) 1345.
[47] M. Terrones, P.M. Ajayan, F. Banhart, X. Blase, D.L. Carroll, J.C. Charlier, R. Czerw, B. Foley, N. Grobert, R. Kamalakaran, P. Kohler-Redlich, M. Ruhle, T. Seeger, H. Terrones, Appl. Phys. A: Mater. Sci. Process. 74 (2002) 355.
[48] B.G. Sumpter, V. Meunier, J.M. Romo-Herrera, E. Cruz-Silva, D.A. Cullen, H. Terrones, D.J. Smith, M. Terrones, ACS Nano 1 (2007) 369.
[49] A. Hashimoto, H. Yorimitsu, K. Ajima, K. Suenaga, H. Isobe, A. Miyawaki, M. Yudasaka, S. Iijima, E. Nakamura, Proc. Natl. Acad. Sci. U.S.A. 101 (2004) 8527.
[50] B.L. Allen, P.D. Kichambare, A. Star, Acs Nano 2 (2008) 1914.
[51] X. Ma, E.G. Wang, R.D. Tilley, D.A. Jefferson, W. Zhou, Appl. Phys. Lett. 77 (2000) 4136.
[52] M.K. Geno, J. Halpern, J. Am. Chem. Soc. 109 (1987) 1238.
[53] J.K.M. Sanders, N. Bampos, Z. Clyde-Watson, S.L. Darling, J.C. Hawley, H.J. Kim, C.C. Mak, S.J. Webb, The Porphyrin Handbook, Academic Press, San Diego, CA, 1999.
[54] A.B.P. Lever, J.P. Wilshire, Can. J. Chem. 54 (1976) 2514.
[55] S.Q. Ma, H.C. Zhou, J. Am. Chem. Soc. 128 (2006) 11734.
[56] I. Barth, J. Manz, Ang. Chem. Int. Ed. 45 (2006) 2962.
[57] D.S. Hecht, R.J.A. Ramirez, M. Briman, E. Artukovic, K.S. Chichak, J.F. Stoddart, G. Grüner, Nano Lett. 6 (2006) 2031.
[58] M.S. Liao, S. Scheiner, J. Comput. Chem. 23 (2002) 1391.
[59] E.J. Baerends, G. Ricciardi, A. Rosa, S.J.A. van Gisbergen, Coord. Chem. Rev. 230 (2002) 5.
[60] A. Tsuda, A. Osuka, Science 293 (2001) 79.
[61] R. Harada, T. Kojima, Chem. Comm. 6 (2005) 716.
[62] T. Nakanishi, T. Kojima, K. Ohkubo, T. Hasobe, K. Nakayama, S. Fukuzumi, Chem. Mater. 20 (2008) 7492.
[63] S.R. Stoyanov, P. Král, J. Phys. Chem. B 110 (2006) 21480.
[64] S.R. Stoyanov, P. Král, J. Chem. Phys. 129 (2008) 234702.
[65] A. Titov, P. Zapol, P. Král, D.J. Liu, I. Hakim, K. Baishya, L. Curtiss, accepted to JPC (2009).
[66] S.R. Stoyanov, P. Kral, B.Y. Wang, Appl. Phys. Lett. 90 (2007) 153110.
[67] T. Ziegler, Chem. Rev. 91 (1991) 651.
[68] A. Becke, J. Chem. Phys. 98 (1993) 5648.
[69] M.J. Frisch, Gaussian 03 Revision C. 02, Gaussian, Inc, Wallingford, CT, 2004.
[70] J.H. Rodriguez, D.E. Wheeler, J.K. McCusker, J. Am. Chem. Soc. 120 (1998) 12051.
[71] S.R. Stoyanov, J.M. Villegas, A.J. Cruz, L.L. Lockyear, J.H. Reibenspies, D.P. Rillema, J. Chem. Theory Comput. 1 (2005) 95.
[72] D.G. Musaev, K. Morokuma, Y.V. Geletii, C.L. Hill, Inorg. Chem. 43 (2004) 7702.
[73] L.K. Stoll, M.Z. Zgierski, P.M. Kozlowski, J. Phys. Chem. A 107 (2003) 4165.
[74] R. Ditchfield, W.J. Hehre, J.A. Pople, J. Chem. Phys. 54 (1971) 724.
[75] A.D. Mclean, G.S. Chandler, J. Chem. Phys. 72 (1980) 5639.
[76] R. Krishnan, J.S. Binkley, R. Seeger, J.A. Pople, J. Chem. Phys. 72 (1980) 650.
[77] K.A. Nguyen, R. Pachter, J. Chem. Phys. 114 (2001) 10757.
[78] J. Mack, Y. Asano, N. Kobayashi, M.J. Stillman, J. Am. Chem. Soc. 127 (2005) 17697.

[79] M. Dolg, U. Wedig, H. Stoll, H. Preuss, J. Chem. Phys. 86 (1987) 866.
[80] D. Andrae, U. Haussermann, M. Dolg, H. Stoll, H. Preuss, Theor. Chim. Acta 78 (1991) 247.
[81] J.S. Binkley, J.A. Pople, W.J. Hehre, J. Am. Chem. Soc. 102 (1980) 939.
[82] E.D. Glendening, A.E. Reed, J. E. Carpenter, F. Wienhold, NBO version 3.1.
[83] ADF program package, version 2003.01: E.J. Baerends, D.E. Ellis, P. Ros, Chem. Phys. 2 (1973) 41.
[84] G. Velde, E. Baerends, J. Comp. Phys. 99 (1992) 84.
[85] G.T. Velde, F.M. Bickelhaupt, E.J. Baerends, C.F. Guerra, S.J.A. Van Gisbergen, J.G. Snijders, T. Ziegler, J. Comput. Chem. 22 (2001) 931.
[86] C.F. Guerra, J.G. Snijders, G. te Velde, E.J. Baerends, Theor. Chem. Acc. 99 (1998) 391.
[87] ADF2004.01, SCM, Theoretical Chemistry, Vrije Universiteit: Amsterdam, The Netherlands, http://www.scm.com.
[88] J.J. Rehr, J.M. Deleon, S.I. Zabinsky, R.C. Albers, J. Am. Chem. Soc. 113 (1991) 5135.
[89] H.S. Kang, S. Jeong, Phys. Rev. B 70 (2004) 233411.
[90] J. Yang, D.J. Liu, Carbon 45 (2007) 2845.
[91] P.H. Matter, E. Wang, M. Arias, E.J. Biddinger, U.S. Ozkan, J. Mol. Catal. A 264 (2007) 73.
[92] Z. Shi, J.J. Zhang, J. Phys. Chem. C 111 (2007) 7084.
[93] M. Sternberg, L.A. Curtiss, D.M. Gruen, G. Kedziora, D.A. Horner, P.C. Redfern, P. Zapol, Phys. Rev. Lett. 96 (2006) 075506.
[94] J.Y. Yi, J. Bernholc, Phys. Rev. B 47 (1993) 1708.
[95] M.H. Ge, K. Sattler, Chem. Phys. Lett. 220 (1994) 192.
[96] J.¡In¿. Subramanian, K.M. Smith, in: Porphyrins and Metalloporphyrins, Elsevier Scientific, Amsterdam, 1975.
[97] D.C. Young, Computational Chemistry: A Practical Guide for Applying Techniquies to Real World Problems, John Willey & Sons, Inc, New York, NY, 2001, pp. 227–228.
[98] W. Jentzen, I. TurowskaTyrk, W.R. Scheidt, J.A. Shelnutt, Inorg. Chem. 35 (1996) 3559.
[99] G.J. Bodwell, J.J. Fleming, M.R. Mannion, D.O. Miller, J. Org. Chem. 65 (2000) 5360.
[100] L.J. Zompa, T.N. Margulis, Inorg. Chim. Acta 28 (1978) 157.
[101] J. Cioslowski, Electronic Structure Calculations on fullerenes and their derivatives, Oxford University Press, New York, 1995.
[102] R.W. Alder, J.N. Harvey, P.V. Schleyer, D. Moran, Org. Lett. 3 (2001) 3233.
[103] J. Pattanayak, T. Kar, S. Scheiner, J. Phys. Chem. A 108 (2004) 7681.
[104] B.C. Guo, K.P. Kerns, A.W. Castleman, Science 255 (1992) 1411.
[105] B.C. Guo, S. Wei, J. Purnell, S. Buzza, A.W. Castleman, Science 256 (1992) 515.
[106] J.M. Lightstone, H.A. Mann, M. Wu, P.M. Johnson, M.G. White, J. Phys. Chem. B 107 (2003) 10359.
[107] C. Zhang, W. Sun, Z. Cao, J. Chem. Phys. 126 (2007) 144306.
[108] P. Liu, J.M. Lightstone, M.J. Patterson, J.A. Rodriguez, J.T. Muckerman, M.G. White, J. Phys. Chem. B 110 (2006) 7449.
[109] K.S. Troche, V.R. Coluci, R. Rurali, D.S. Galvao, J. Phys. -Cond. Matt. 19 (2007) 236222.
[110] M. Matsubara, C. Massobrio, Mater. Sci. Eng. C: Biomim. Supramolec. Sys. 26 (2006) 1224.
[111] J.Q. Hou, H.S. Kang, Chem. Phys. 334 (2007) 29.
[112] J.F. Christian, Z.M. Wan, S.L. Anderson, J. Phys. Chem. 96 (1992) 10597.
[113] U. Reuther, A. Hirsch, Carbon 38 (2000) 1539.
[114] F. Fulop, A. Rockenbauer, F. Simon, S. Pekker, L. Korecz, S. Garaj, A. Janossy, Chem. Phys. Lett. 334 (2001) 233.
[115] H. Shinohara, Rep. Prog. Phys. 63 (2000) 843.
[116] J. Lee, H. Kim, S.J. Kahng, G. Kim, Y.W. Son, J. Ihm, H. Kato, Z.W. Wang, T. Okazaki, H. Shinohara, Y. Kuk, Nature 415 (2002) 1005.
[117] I. Narita, T. Oku, Diamond And Related Materials 12 (2003) 1146.
[118] D.P. Rillema, R. Sahai, P. Matthews, A.K. Edwards, R.J. Shaver, L. Morgan, Inorg. Chem. 29 (1990) 167.
[119] B. Paulus, Phys. Chem. Chem. Phys. 5 (2003) 3364.
[120] Z.Y. Wang, K.H. Su, H.Q. Fan, L.D. Hu, X. Wang, Y.L. Li, Z.Y. Wen, Comp. Mater. Sc. 40 (2007) 537.
[121] L.F. Yuan, J. Yang, K. Deng, Q.S. Zhu, J. PHys. Chem. A 104 (2000) 6666.
[122] M.N. Jagadeesh, J. Chandrasekhar, Chem. Phys. Lett. 305 (1999) 298.
[123] T. Kalai, B. Bognar, J. Jeko, K. Hideg, Synthesis (2006), P06406SS.
[124] D. Shultz, Polyhedron 20 (2001) 1627.
[125] T. Kambe, K. Kajiyoshi, M. Fujiwara, K. Oshima, Phys. Rev. Lett. 99 (2007) 177205.
[126] J. Simaan, S. Poussereau, G. Blondin, J.J. Girerd, D. Defaye, C. Philouze, J. Guilhem, L. Tchertanov, Inorg. Chim. Acta 299 (2000) 221.
[127] Z.Y. Wu, Y. Tao, M. Benfatto, D.C. Xian, J.Z. Jiang, J. Synchrotron Rad. 12 (2005) 98.
[128] R.J. Barton, R.W. Dabeka, S.G. Hu, L.M. Mihichuk, M. Pizzey, B.E. Robertson, W.J. Wallace, Acta Crystallogr. C 39 (1983) 714.
[129] P.G. Edwards, M.B. Hursthouse, K.M.A. Malik, J.S. Parry, J. Chem. Soc. 10 (1994) 1249.
[130] M.G. Schultz, T. Diehl, G.P. Brasseur, W. Zittel, Science 302 (2003) 624.
[131] B. Wang, J. Power Sources 152 (2005) 1.
[132] S. Mukerjee, S. Srinivasan, A.J. Appleby, Electrochim. Acta 38 (1993) 1661.
[133] H.Q. Li, G.Q. Sun, N. Li, S.G. Sun, D.S. Su, Q. Xin, J. Phys. Chem. C 111 (2007) 5605.
[134] J.L. Fernandez, D.A. Walsh, A.J. Bard, J. Am. Chem. Soc. 127 (2005) 357.
[135] V. Stamenkovic, T.J. Schmidt, P.N. Ross, N.M. Markovic, J. Electroanal. Chem. 554 (2003) 191.
[136] F. Studt, F. Abild-Pedersen, T. Bligaard, R.Z. Sorensen, C.H. Christensen, J.K. Norskov, Science 320 (2008) 1320.
[137] S. Enthaler, K. Junge, M. Beller, Angew. Chem. Int. Ed. 47 (2008) 3317.
[138] J. Yang, D.J. Liu, N.N. Kariuki, L.X. Chen, Chem. Commun. 3 (2008) 329.
[139] S. Kim, T. Ohta, G. Kwag, Bull. Korean Chem. Soc. 21 (2000) 588.
[140] J. Berkowitz, J. Chem. Phys. 70 (1979) 2819.
[141] R. Gao, Z. Pan, Z.L. Wang, Appl. Phys. Lett. 78 (2001) 1757.
[142] T. Gallagher, Rydberg Atoms, Cambridge University Press, New York, 1994.
[143] C.H. Greene, A.S. Dickinson, H.R. Sadeghpour, Phys Rev Lett 85 (2000) 2458.
[144] B.E. Granger, P. Král, H.R. Sadeghpour, M. Shapiro, Phys. Rev. Lett. 89 (2002) 135506.
[145] D. Segal, B.E. Granger, H.R. Sadeghpour, P. Král, M. Shapiro, Phys. Rev. Lett. 94 (2005) 016402.
[146] M. Zamkov, N. Woody, S. Bing, H.S. Chakraborty, Z. Chang, U. Thumm, P. Richard, Phys. Rev. Lett. 93 (2004) 156803.
[147] A. Davidov, Quantum Mechanics, Pergamon, Oxford, UK, 1965.
[148] C. Kim, B. Kim, S.M. Lee, C. Jo, Y.H. Lee, Appl. Phys. Lett. 79 (2001) 1187.
[149] C. Kim, B. Kim, S.M. Lee, C. Jo, Y.H. Lee, Phys. Rev. B 65 (2002) 165418.
[150] J.M. Bonard, K.A. Dean, B.F. Coll, C. Klinke, Phys. Rev. Lett. 89 (2002) 197602.
[151] Y.C. Choi, W.Y. Kim, K.S. Park, P. Tarakeshwar, K.S. Kim, T.S. Kim, J.Y. Lee, J. Chem. Phys. 122 (2005) 094706.
[152] S.I. Themelis, C.A. Nicolaides, J. Phys. B: At. Mol. Opt. Phys. 34 (2001) 2905.
[153] M. Ishigami, J.D. Sau, S. Aloni, M.L. Cohen, A. Zettl, Phys. Rev. Lett. 94 (2005) 056804.
[154] K. Becker, J.M. Lupton, J. Muller, A.L. Rogach, D.V. Talapin, H. Weller, J. Feldmann, Nat. Mater. 5 (2006) 777.
[155] T. Kuzumaki, Y. Takamura, H. Ichinose, Y. Horiike, Appl. Phys. Lett. 78 (2001) 3699.
[156] K.A. Dean, B.R. Chalamala, Appl. Phys. Lett. 76 (2000) 375.
[157] J. Cumings, A. Zettl, M.R. McCartney, J.C.H. Spence, Phys. Rev. Lett. 88 (2002) 056804.
[158] G. Binnig, H. Rohrer, IBM J. Res. Dev. 30 (1986) 355.
[159] A.S. Duwez, S. Cuenot, C. Jèrôme, S. Gabriel, R. Jèrôme, S. Rapino, F. Zerbetto, Nat. Nanotechnol. 1 (2006) 122.
[160] B.Y. Wang, P. Král, J. Am. Chem. Soc. 128 (2006) 15984.
[161] V. Balzani, A. Juris, M. Venturi, S. Campagna, S. Serroni, Chem. Rev. 96 (1996) 759.
[162] S.R. Stoyanov, J.M. Villegas, D.P. Rillema, Inorg. Chem. 41 (2002) 2941.
[163] J.P. Collman, J.T. Mcdevitt, G.T. Yee, C.R. Leidner, L.G. Mccullough, W.A. Little, J.B. Torrance, Proc. Natl. Acad. Sci. 83 (1986) 4581.
[164] G.J. Meyer, Inorg. Chem. 44 (2005) 6852.
[165] C.Y. Chen, S.J. Wu, C.G. Wu, J.G. Chen, K.C. Ho, Angew. Chem. Int. Ed. 45 (2006) 5822.
[166] S. Peng, K.J. Cho, Nano Lett. 3 (2003) 513.
[167] P. Gauden, M. Wisniewski, Appl. Surf. Sci. 253 (2007) 5726.
[168] A. Galano, Chem. Phys. 327 (2006) 159.
[169] F.F. Contreras-Torres, V.A. Basiuk, E.V. Basiuk, J. Phys. Chem. A 112 (2008) 8154.
[170] K. Choho, W. Langenaeker, G. Van de Woude, P. Geerlings, J. Mol. Struct. (Theochem.) 362 (1996) 305.
[171] A. Alfarra, E. Frackowiak, F. Bguin, Appl. Surf. Sci. 228 (2004) 84.
[172] M. Yu, Z. Li, Q. Xia, H. Xi, S. Wang, Chem. Eng. J. 132 (2007) 233.
[173] A.R. Terzyk, M. Wisniewski, P.A. Gauden, G. Rychficki, S. Furmaniak, J. Colloid Interface Sci. 320 (2008) 40.
[174] S.R. Stoyanov, S. Gusarov, S.M. Kuznicki, A. Kovalenko, J. Chem. Phys. C 112 (2008) 6794.
[175] S.R. Stoyanov, S. Gusarov, A. Kovalenko, Molec. Simulation Spec. Iss. Materials Studio 34 (2008) 953.
[176] P. Král, Phys. Rev. B 66 (2002) 241401.
[177] S.S. Wong, A.T. Woolley, E. Joselevich, C.M. Lieber, Chem. Phys. Lett. 306 (1999) 219.
[178] K. Komatsu, M. Murata, Y. Murata, Science 307 (2005) 238.
[179] L.T. Scott, M.M. Boorum, B.J. McMahon, S. Hagen, J. Mack, J. Blank, H. Wegner, A. de Meijere, Science 295 (2002) 1500.
[180] Y. Rubin, T. Jarrosson, G.W. Wang, M.D. Bartberger, K.N. Houk, G. Schick, M. Saunders, R.J. Cross, Ang. Chem. Int. Ed. 40 (2001) 1543.
[181] M. Machado, P. Piquini, R. Mota, Chem. Phys. Lett. 392 (2004) 428.
[182] J. Antesberger, G.W.V. Cave, M.C. Ferrarelli, M.W. Heaven, C.L. Atwood, J.L. Raston, Chem. Comm. 7 (2005) 892.